THERMALLY INDUCED VIBRATIONS OF A SOLAR WING WITH BOWED STEM

A Thesis

by

SHAWN AVERY HAGLER

Submitted to the Office of Graduate Studies of
Texas A&M University
in partial fulfillment of the requirements for the degree of

MASTER OF SCIENCE

December 2010

Major Subject: Mechanical Engineering

THERMALLY INDUCED VIBRATIONS OF A SOLAR WING WITH BOWED STEM

A Thesis

by

SHAWN AVERY HAGLER

Submitted to the Office of Graduate Studies of
Texas A&M University
in partial fulfillment of the requirements for the degree of

MASTER OF SCIENCE

Approved by:

Chair of Committee,	Alan Palazzolo
Committee Members,	Michael Schuller
	William Schneider
Head of Department,	Dennis O'Nea1

December 2010

Major Subject: Mechanical Engineering

ABSTRACT

Thermally Induced Vibrations of a Solar Wing with Bowed STEM. (December 2010)

Shawn Avery Hagler, B.S., Texas A&M University

Chair of Advisory Committee: Dr. Alan Palazzolo

Storable Tubular Extendible Members (STEMs) are often used for deploying spacecraft subsystems such as flexible solar cell blankets, like those used on Hubble Telescope. Systems using long flexible appendages such as the STEMs used on Hubble often undergo thermal excitations due to a thermal gradient through the cross-section when entering and exiting solar eclipse. These vibrations can greatly reduce pointing accuracy and lead to mission failure.

Boeing obtained a patent in 2006 for the High Power Thin Film Solar Array (HPSA) which could provide 130kW of power to a spacecraft. The deployed structure relies on bowed STEMs and a tether system to keep the solar panels taut and in alignment with the sun. The system is predicted to minimize the effects of thermal excitation.

This thesis proves that the HPSA design can outperform its straight STEM counterparts with respect to thermal-structural stability under unidirectional solar radiant heating through the use of finite element models created in ANSYS. In comparison to Hubble, a HPSA wing configuration is capable of providing a 44.5% increase in the first

modal frequency, a 98.8% reduction in steady state tip deflection, and 96.9% reduction in tip vibration amplitude.

TABLE OF CONTENTS

Page

ABSTRACT iii

TABLE OF CONTENTS v

LIST OF FIGURES vii

LIST OF TABLES x

1. INTRODUCTION 1

1.1. Statement of Thesis 4
1.2. Literature Review 4
1.3. Objectives and Novel Contribution 7

2. STRUCTURAL CHARACTERIZATION OF THE BOWED STEM 8

2.1. Introduction 8
2.2. Analysis 10
2.3. Force Output 12
2.4. Identification of HPSA STEM Properties 13
2.5. Summary 15

3. THERMAL CHARACTERIZATION OF THE STEM CROSS SECTION 16

3.1. Introduction 16
3.2. Simplification of the Temperature Profile 17
3.3. Full Thermal Model vs. the Simplified Thermal Model 21
3.3.1. Thermal Steady State Analysis of the STEM Profile 23
3.3.2. Thermal Transient Analysis of the STEM Profile 24
3.4. Model Comparison 27
3.5. Summary 27

4. UNDER UNIDIRECTIONAL SOLAR RADIANT HEAT 28

4.1. Single Solar Wing Considerations 28
4.2. Model Description 28
4.3. Solution Algorithm 30
4.4. Validation of Algorithm 34

Page

4.5. Parameters and Assumptions 37
4.5.1. Spreader Bar Mass....38
4.5.2. Panel Tension for Straight STEM Equivalent....39
4.5.1. Tether Properties 39
4.5.2. Solar Panel Properties....41

5. RESULTS....43

5.1. Modal Analysis 43
5.2. Coupled Thermal-Structural Steady State Analysis....46
5.3. Coupled Thermal-Structural Transient Analysis....49
5.3.1. Hubble 50
5.3.1. Straight STEM Equivalent 51
5.3.2. HPSA Configuration 2 53
5.3.3. HPSA Configuration 3 55
5.3.4. Comparison....57
5.4. Effects of Damping on HPSA Transient Response....58

6. CONCLUSIONS AND RECOMMENDATIONS....62

6.1. Conclusion....62
6.2. Recommendations 62

REFERENCES....63

VITA 65

LIST OF FIGURES

Page

Figure 1. Diagram of a deploying STEM system [1] 2

Figure 2. Picture of deployed HPSA assembly [2] 3

Figure 3. Diagram of the HPSA Tether/Bow STEM system [2] 3

Figure 4. Diagram showing Bow STEM configuration parameters 9

Figure 5. Non-dimensional Bow STEM output force plotted against cord height 12

Figure 6. Bow STEM output force plotted against cord height 15

Figure 7. Diagram of STEM cross section with heat flux applied. 18

Figure 8. Steady state temperature profile for the STEM 23

Figure 9. Comparison of the FEA steady state temperature distribution compared to the 1st order approximated solution 24

Figure 10. Transient temperatures for the top and bottom of the Bow Beam predicted by ANSYS 25

Figure 11. Comparison of the transient temperature difference for the full model and 1st order approximation model over 4000 seconds (top) and 500 seconds (bottom) 26

Figure 12. Flow chart for the multiple physics solution algorithm 32

Figure 13. Diagram of temperature loads for a 2D beam in ANSYS. 33

Figure 14. Stable HST tip deflection 35

Figure 15. Unstable HST tip deflection 36

Figure 16. Marginally stable HST tip deflection 36

Figure 17. Mode shapes for each design with the largest tip deflection plotted in ANSYS. 45

Page

Figure 18. Steady state deflection in the Y along the straight STEM 47

Figure 19. Steady state average temperatures along the length of the STEM.....48

Figure 20. Steady state perturbation temperatures along the length of the STEM 49

Figure 21. HST tip displacement histories for 0˚ (left) and 80˚ (right) incident angles 50

Figure 22. HST tip velocity histories for 0˚ (left) and 80˚ (right) incident angles 51

Figure 23. HST tip velocity FFTs for 0˚ (left) and 80˚ (right) incident angles 51

Figure 24. SSE tip displacement histories for 0˚ (left) and 80˚ (right) incident angles 52

Figure 25. SSE tip velocity histories for 0˚ (left) and 80˚ (right) incident angles 52

Figure 26. SSE tip velocity FFTs for 0˚ (left) and 80˚ (right) incident angles.....53

Figure 27. HPSA2 tether tension histories for 0˚ (left) and 80˚ (right) incident angles 54

Figure 28. HPSA2 tip displacement histories for 0˚ (left) and 80˚ (right) incident angles 54

Figure 29. HPSA2 tip velocity histories for 0˚ (left) and 80˚ (right) incident angles 55

Figure 30. HPSA2 tip velocity FFTs for 0˚ (left) and 80˚ (right) incident angles 55

Figure 31. HPSA3 tether tension histories for 0˚ (left) and 80˚ (right) incident angles 56

Figure 32. HPSA3 tip displacement histories for 0˚ (left) and 80˚ (right) incident angles 56

Figure 33. HPSA3 tip velocity histories for 0˚ (left) and 80˚ (right) incident angles 57

Page

Figure 34. HPSA3 tip velocity FFTs for 0˚ (left) and 80˚ (right) incident angles 57

Figure 35. Tip velocity history for HPSA2 with 0˚ incident angle applied 59

Figure 36. Tip velocity history for HPSA2 with 80˚ incident angle applied 60

Figure 37. Tip velocity history for HPSA3 with 0˚ incident angle applied 61

Figure 38. Tip velocity history for HPSA3 with 80˚ incident angle applied 61

LIST OF TABLES

Page

Table 1. Parameters for the structural bow STEM analyses 11

Table 2. Parameters used in thermal steady state and thermal transient analyses 22

Table 3. List of parameters used in wing simulations.....37

Table 4. Assumed Kevlar material properties.....41

Table 5. Material properties from Matweb ™ for "DuPont™ Kapton® 50HN Polyimide Film, 13 Micron Thickness”[16].....42

Table 6. First ten modes of each solar wing configuration 44

Table 7. First ten nondimensionalized modes of each solar wing configuration 46

Table 8. Comparison between wing configurations.....58

1. INTRODUCTION

Storable Tubular Extendible Members (STEMs) are often used for deploying spacecraft subsystems such as flexible solar cell blankets, like those used on Hubble Telescope. STEMs are beam-like structures that are capable of being stored on a reel, and are similar to a carpenter's tape measure. As the STEM is extended from its reel, it transitions from a flattened to tubular profile. A diagram of a STEM deployment system can be seen in Figure 1.

Bending due to thermal gradient through the cross-section is a major problem effecting STEMs when used on space structures. These thermal gradients are due unidirectional solar radiant heat. Along with a static deflection, an oscillation can be excited by sudden changes in the thermal gradients. This oscillation is known as a thermally induced vibration. As demonstrated by the Hubble Telescope when it was first put into orbit, these vibrations can drastically reduce pointing accuracy of the satellite.

This thesis follows the style of Journal of Computational and Nonlinear Dynamics.

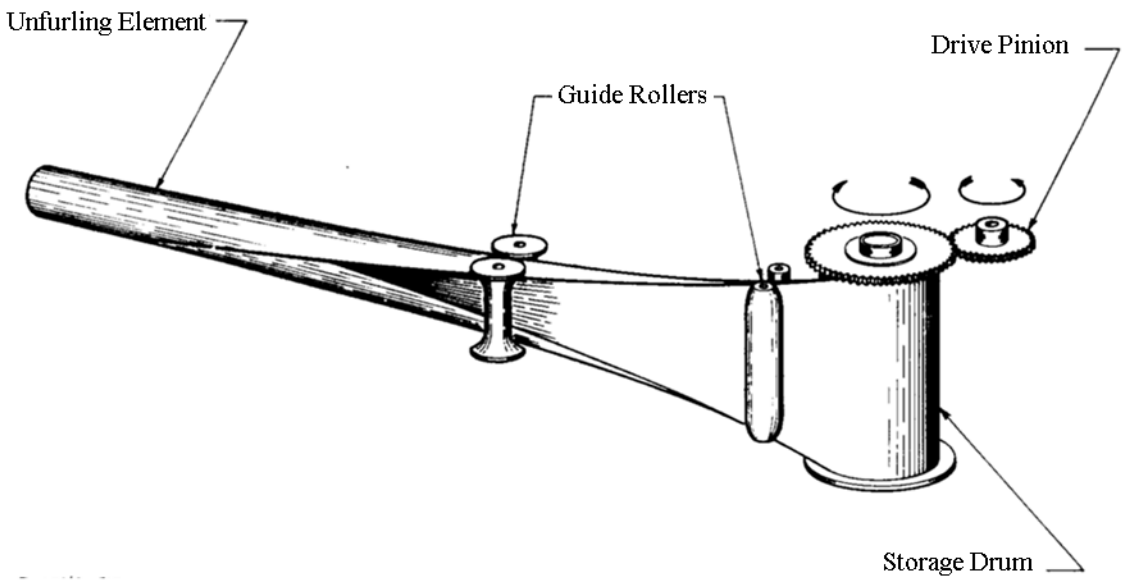

Figure 1. Diagram of a deploying STEM system [1]

Boeing has come up with a new concept with the main intent being the reduction of both thermally induced vibrations and static deflection of the STEM dependent solar wings. The High Performance Solar Array (HPSA) utilizes bowed STEMs (Bow Beams) and a system of tethers to deploy two solar wings. A picture of the deployed HPSA structure can be seen in Figure 2. The HPSA structure uses the tethers to provide both vertical and horizontal stiffness. The Bow Beams function as weak (almost constant force) compressive springs which load the system and keep the solar panels and tethers taut. This system is designed to make the tip of the Solar Wing dependent on the geometry of the tethers rather than the temperature gradient through STEM cross-section [2].

A single HPSA module includes both two solar panel sheets, two spools which maintain panel tension, two spreader bars at the tip of each wing, four bowed STEM's to provide outward force on the spreader bars, four vertical tether beams, and eight tethers which provide vertical stiffness to the wing tips. A diagram of the HPSA can be seen in Figure 3. The initial design includes a nominal panel tension of 2.0 lbs, nominal Bow STEM force of 1.5 lbs each, panel length of 50 ft, panel width of 141 in.

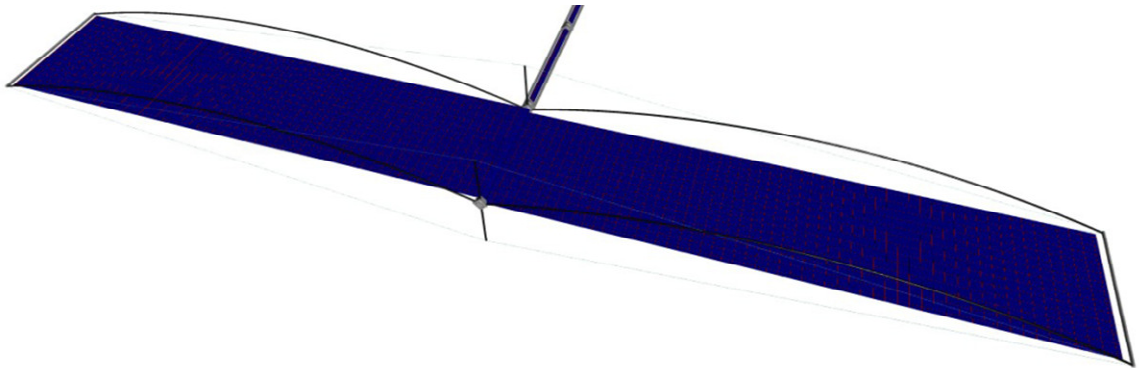

Figure 2. Picture of deployed HPSA assembly [2]

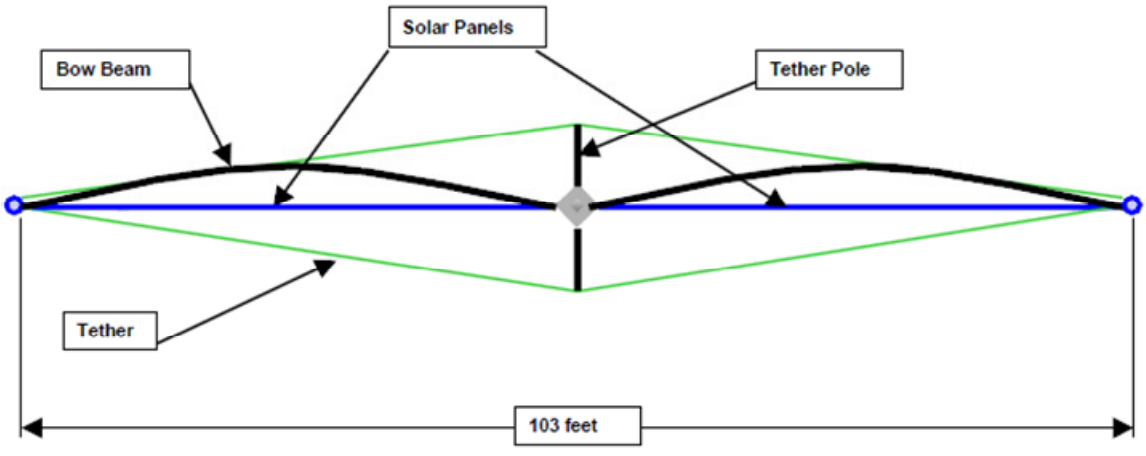

Figure 3. Diagram of the HPSA Tether/Bow STEM system [2]

1.1. Statement of Thesis

The author's thesis is that *the High Power Solar Array design can outperform its straight STEM counterparts with respect to thermal-structural stability under unidirectional solar radiant heating.* The purpose of this paper is to investigate the structural characteristics of the bowed STEM, evaluate the performance of the HPSA design under unidirectional solar radiant heating, and prove the author's thesis.

1.2. Literature Review

The history of Storable Tubular Extendible Members (STEMs) started in 1960 with the Special Products and Applied Research Division of Havilland Aircraft of Canada Limited when they were selected by the Defense Research Telecommunications Establishment to perform the structural and mechanical design of the Canadian Topside Sounder Satellite. The extendible member principle was originally selected for providing the necessary lengths for sounding antennas and has since culminated into the STEM devices being utilized for flexible solar panel deployment [1] .

In 1968, Augusti studied dynamic instability (thermal flutter) in two strut models, a one degree of freedom and a two degree of freedom, represented by rigid bars connected by deformable cells constituted by elastic hinges with heat-sensitive plates. This allowed for thermal deformations to be lumped at the joints. The radiant heat source and tip load were both in the axial direction of the strut system. Augusti developed both static (buckling) and dynamic (flutter) stability criteria for the model [3].

Beam then went on to demonstrate thermoelastic instability in a laboratory exercise with a one degree of freedom torsional pendulum in 1969. He predicted that the

thermoelastic coupling of the torsional pendulum with a small amplitude linear analysis [4].

In 1969, Yu performed an analysis on the instability of a beam due to thermal bending. He derived the governing equation from Hamilton's principle by assuming the beam was a solid continuum and that the thermal curvature was linearly related to the local heat input by a first order differential equation [5].

Merrick then developed an analytical model of a cantilevered beam concerned with the influence of thermal bending moments on slender boom stability, both transverse and torsional, in 1970. His model included the following assumptions: thermal torques were negligible, the effective mass was located at the tip ensuring only one bending and one torsional mode of vibration, the cross section was thermally seamless (not necessarily structurally), and boom bending had no effect on the thermal bending moments. Merrick found that initial curvature of the beam in its steady state position can significantly affect stability. Without structural damping, an initially straight boom would be unstable. Bowing toward the radiant heat source aided stability while bowing away only reduced stability [6].

Frisch went on to develop equations for coupled transverse plus torsional vibration of a long, open section, cantilevered cylinder (essentially a STEM) exposed to radiant heat in 1970. Unlike Merrick, Firsch included thermal torques and also the effects of bending on thermal response. He implied that the elastic restoring force should be measured from a time-varying position of static thermal equilibrium rather than its undeflected position because it has a strong component at the first natural

bending frequency which can excite a resonance. Therefore, the thermal and vibration equations are coupled and should be solved simultaneously [7].

In 1989, Murozono and Sumi presented a theoretical analysis of the thermally induced bending vibration of a thin-walled boom with tip mass subjected to unidirectional solar radiant heat where the heat input was dependent on the angle of incidence. They took the heat balance equation in the circumferential direction, and then assumed that the temperature was the sum of an average and perturbation temperature. This allowed for the thermal gradient to be solved for with a first order linear equation (similar to Yu). The governing equations were solved with Laplace transformations and numerical inversions of the transformed solution. They found that stability is highly dependent on angle of incidence of the unidirectional radiant heat source [8].

Thornton described an analytical approach for determining the thermal-structural response of a flexible rolled-up solar array under unidirectional radiant heat which uses thin walled booms for deployment in 1993. Thornton's coupled model, like Murozono and Sumi, also used the perturbation temperature to decouple the gradient from the heat governing equations. Governing equations for the beam and solar blanket were determined by Galerkin's form of the Weighted Residual Method. Inversion of the Laplace transforms was then used to find the solution for the equations [9].

In 2007, Xue Duan and Xiang presented a finite element scheme for solving thermally induced bending-torsion coupling vibration of large scale space structure which utilized thin-walled beam with open and closed cross sections. They developed a beam element which includes average and perturbation temperature degrees of freedom

and calculated incident heat fluxes internally. This set the basis for the use of finite element software in coupled thermal-elastic dynamics of STEM reliant space structures.

Previous literature researches the effects of unidirectional heating on flexible structures; however, none examine a solar wing which utilizes prestressed STEMs in bowed configurations like those used on Boeing's High Power Solar Array.

1.3. Objectives and Novel Contribution

Objectives:

- Characterization of Bow STEM
  - Force output of the Bow STEM
  - Thermal response of the Bow STEM cross section
  - Simplification of the thermal response of the cross section
- Wing Characterization
  - Modal response of a two separate HPSA configurations (HPSA2 and HPSA3) along with HST and a HPSA Straight STEM Equivalent (SSE) for comparison.
  - Steady State Response of the HPSA2, HPSA3, HST, and SSE configurations under unidirectional radiant heating.
  - Transient response of the HPSA2, HPSA3, HST and SSE configurations under unidirectional radiant heating.

Novel contributions of this thesis include:

- Process for identifying necessary cross sectional properties to provide a bow STEM with a predetermined force output and cord height to cord length ratio.
- Modal, Static, and Transient analysis of a solar wing which utilizes prestressed STEMs in bowed configurations.

2. STRUCTURAL CHARACTERIZATION OF THE BOWED STEM

2.1. Introduction

It has become a common practice to utilize straight STEMs to deploy thin film solar arrays where the STEM is loaded axially in compression by the tensioned solar panel. In the straight configuration, the design is limited to the STEM's first buckling mode. Loading the STEMs beyond their buckling load can result in large lateral displacements which can drastically reduce the effectiveness of the solar panel.

By bowing the STEM, the HPSA design positions the beam in a new equilibrium state capable of enduring higher compressive loads in comparison to its straight beam counterpart. This can be seen when examining Euler's formula for the buckling load of columns under axial compression,

$$P_b = \frac{\pi^2 EI}{(KL)^2} \tag{1}$$

where E is the modulus of elasticity, I is the area moment of inertia, K is the effective length factor determined by the boundary conditions, and L is the length of the beam. Assuming that all parameters of the beam are constant, the boundary conditions are what determine the buckling load. In the straight beam configuration, the STEM is fixed at the root and allowed to displace laterally. This type of boundary condition gives the straight beam an effective length of 2.0. A bowed beam would closely resemble a pinned-pinned boundary condition with an effective length of 1.0, and therefore could carry a load four times that of the straight beam. Also the bowed beam would be in a

stable equilibrium position while the straight beam would be unstable at its buckling load.

Assuming that the arc of the bowed beam can be represented by half of a sine curve, the bowed configuration can be completely defined by cord length and cord height as seen in Figure 4 and expressed in (2).

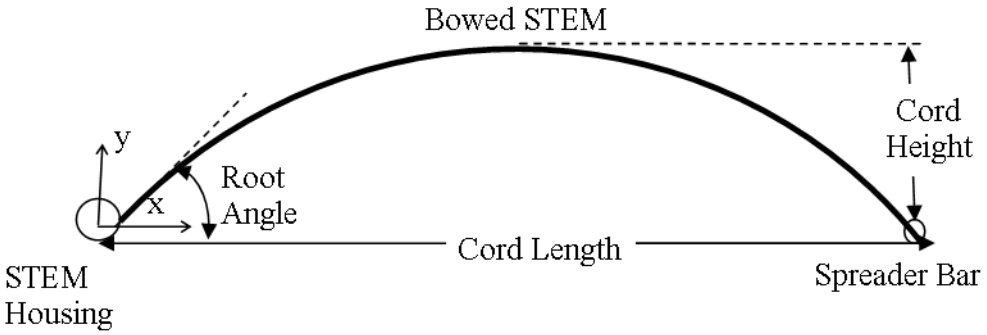

Figure 4. Diagram showing Bow STEM configuration parameters

$$y=H_c \sin\left(\frac{\pi x}{L_c}\right) \tag{2}$$

where H_c is the cord height and L_c is the cord length. The derivative of the curve with respect to x is then:

$$\frac{dy}{dx}=\frac{\pi H_c}{L_c}\cos\left(\frac{\pi x}{L_c}\right) \tag{3}$$

From this equation, the root angle and the arc length of the beam can be found.

$$\theta_{root}=\frac{\pi H_c}{L_c} \tag{4}$$

$$L_{arc} = \int_0^{L_c} \sqrt{1 + \left(\frac{\pi H_c}{L_c} \cos\left(\frac{\pi x}{L_c}\right)\right)^2}\, dx \tag{5}$$

The pinned-pinned buckling load can be used to approximate the bowed STEM output force used to keep the tethers and solar panel tensioned. However, the beam may not actually be able to carry the full buckling load. The beams output force is dependent upon both properties of the beam and its bowed configuration.

A 2D nonlinear structural analysis was created with the intent of determining the force output with respect to its bowed amplitude. A description of the analysis can be seen in the sections that follow.

2.2. Analysis

The 2D structural model is made up of beam elements in an arc with the distance between end points being considered the cord length. The beam is initially deflected at its center by a small amount in the analysis to ensure that the beam bows in the correct direction. A small initial deflection was chosen, 2.54mm (0.1 in), as to obtain a more accurate force response. Its arc length is set by (5) to provide the correct final cord length and cord height. Change in arc length due to axial compression of the STEM is assumed to be negligible.

Boundary conditions are applied at the ends of the beams. The end furthest from the origin has fixed displacements in the x and y while being free to rotate in the z. The end closest to the origin has similar boundary conditions, but it's displaced in the +x direction an amount equal to the difference between the arc length and the final cord length allowing the beam to bow.

$$u_x(L_{arc})=u_y(0)=u_y(L_{arc})=0 \qquad (6)$$
$$u_x(0)=L_{arc}-L_{cord}$$

Boeing provides a description of the bowed STEM arc including cord height and cord length, but there is very little description of the STEM itself. Since all of the necessary properties for the bowed STEM are unknown, general Hubble values are initially assumed where needed. After results for the Hubble STEM were collected, a second cross section was created to provide the necessary output force of 1 lb called for by the HPSA design. All parameters are shown in Table 1.

Table 1. Parameters for the structural bow STEM analyses

	Value			
Parameter	Hubble	HPSA	Unit	Description
A	1.610E-05	1.544E-05	m^2	cross sectional area
E	1.930E+11		N/m^2	modulus of elasticity
h	2.35E-04		m	thickness
H_c	1.524		m	cord height
H_i	2.54E-03		m	initial height
I	8.870E-10	8.448E-10	m	area moment of inertia
L_{arc}	15.61		m	arc length
L_c	15.24		m	cord length
P	7.270E+00	6.929E+00	N	buckling load
R	1.092E-02	1.058E-02	m	radius
η_{xy}	0.3			Poisson's ratio

2.3. Force Output

The reaction force at the root is recovered from the analysis to provide an accurate force output for the bowed STEM. By also recording the y displacement at the center of the STEM, the force output can be related to the bowed configuration, or cord height to cord length ratio. The nonlinear force output for the two bow STEM's are present in Figure 5. The first curve is for the Hubble STEM, and the second is for the HPSA STEM, which will be discussed in the next section, lies directly on top of the previous curve.

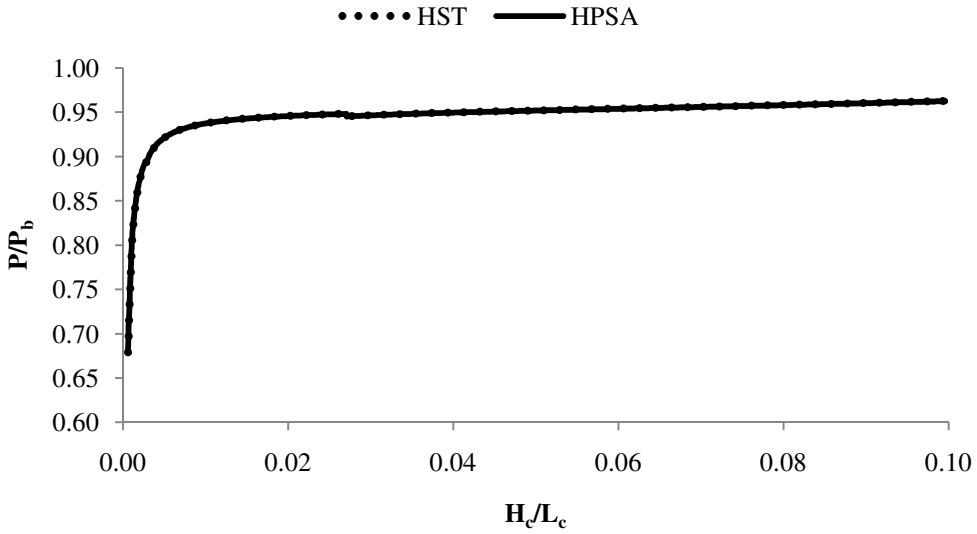

Figure 5. Non-dimensional Bow STEM output force plotted against cord height

The curves show buckling occurring at a cord height that is 1.1% of the cord length. After this buckling point, the beam becomes much less stiff. This drop in

stiffness shows that the beam has reached a new equilibrium position in its bowed state. The bowed beam acts like a weak (constant force) spring in this configuration. The output force is about 96.3% that of the predicted buckling force (7.28 N for Hubble and 6.67 N for HPSA) with a cord height at 10% of the cord length. Assuming that the non-dimensional curve applies to other beam configurations, STEM properties can be approximated by knowing the necessary output force and cord height to cord length ratio.

2.4. Identification of HPSA STEM Properties

As stated previously, Boeing did not specify parameters for the bowed STEM. A 6.67 N (1.5 lb) output force is all that is required for by the HPSA design. Using the factor from the curve in Figure 5, an Euler buckling load can be selected

$$P_b = \frac{P}{\left(\frac{P}{P_b}\right)_{curve}} \tag{7}$$

where P=6.67 N and $\left(\frac{P}{P_b}\right)_{curve}$=0.963 for the HPSA design. Therefore the buckling load for the HPSA STEM (previously shown in Table 1) is calculated to be 6.93 N. With the buckling load, (1) can be rearranged to solve for the area moment of inertia.

$$I = \frac{P_b (KL)^2}{\pi^2 E} \tag{8}$$

Assuming that modulus of elasticity from Hubble, the pinned-pinned effective length, and the 15.24 m cord length provided by Boeing, the area moment of inertia is found to be 8.448E-10 m^4. The area moment of inertia of a tube is provided in the equation below.

$$I_{tube}=\frac{\pi\left(R^4-(R-h)^4\right)}{4} \tag{9}$$

where h is the thickness of the tube and R is the radius. Using the area moment of inertia found by (8) and assuming the thickness of the Hubble STEM (2.35e-4 m), the radius of the tube is found to be 1.058E-2 m. Last, the area of the STEM is found to be 1.544E-05 m^2 calculated using (10).

$$A_{tube}=\pi(R^2-(R-h)^2) \tag{10}$$

Now the necessary cross sectional properties for the STEM are provided for the HPSA design, and the analysis is performed again. The non-dimensional force output for the HPSA design is presented in the previously shown Figure 5. The assumption that the non-dimensional curve applies to other beam configurations is confirmed by the overlap of the Hubble and HPSA curves.

The same two curves for Hubble and HPSA are plotted with force units against cord height in Figure 6. The HPSA force output reaches 1.673 lb at a cord height of 1.515 m. Therefore using the 0.963 factor with the Euler Buckling provides a beam which is only 0.02% from the design load. Also, the assumption that the change in arc length is negligible is confirmed by the model cord height being only 0.6% less than the design height. Had drastic changes in arc length occurred, the error would have been larger.

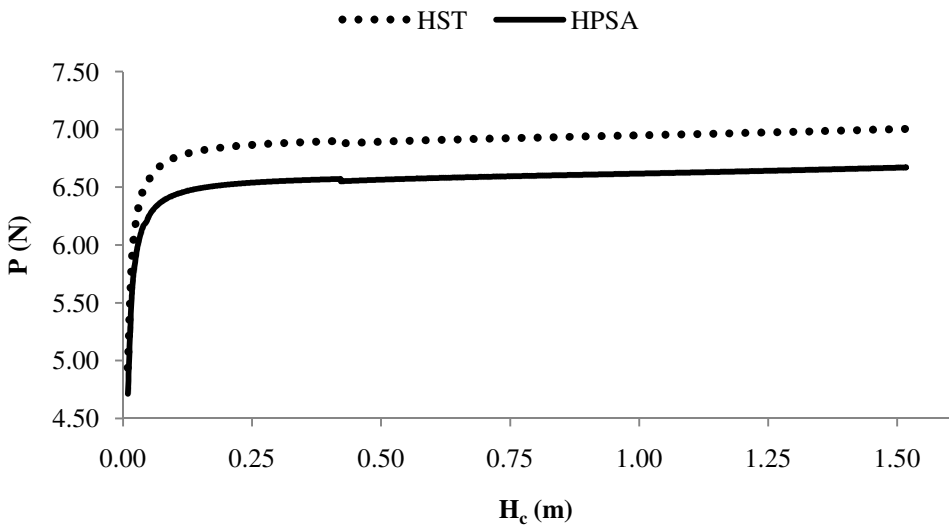

Figure 6. Bow STEM output force plotted against cord height

2.5. Summary

- The arc of the Bow STEM can be represented half of a sine curve with (2).
- The output force of the Bow STEM can be effectively approximated by the pinned-pinned Euler buckling and factor that is a function of the design load and cord height to cord length ratio from a non-dimensional force curve like Figure 5.
- A Bow STEM with the following tube cross sectional properties should be able to produce the necessary 6.67 N output force required by the HPSA design assuming the same material properties as the Hubble STEM:
    - Radius of 1.058 cm
    - Thickness of 0.235 mm
    - Cross Sectional Area of 1.544E-05 m^2
    - Area Moment of Inertia of 8.448E-10 m^4

3. THERMAL CHARACTERIZATION OF THE STEM CROSS SECTION

3.1. Introduction

As stated earlier, unidirectional radiant solar heating of a STEM causes a temperature gradient through the cross section, and thermal snap is a direct response to that gradient. In order to accurately simulate the coupled thermal response of a snap, a means of effectively modeling this cross sectional temperature gradient is necessary.

Traditional methods of coupled structural-thermal interactions are often modeled through the use of plane, solid, and shell elements where meshes overlap between thermal and structural physics. However in the case of slender beam structures, these elements often would require high nodal and degree of freedom counts in order to provide both cross sectional and axial temperatures. Because of this, computational time and memory tend to be larger than ideal.

Another option would be to replace the structural model with beam elements which should drastically reduce structural nodal count. This requires a means of transferring displacements and temperatures between the two different meshes, the structural and thermal. This task can be extremely difficult if there's not a direct link between the structural and thermal meshes. One way to create this direct link would be to make a set of cross sectional thermal nodes for every beam node. Gradients could then be transferred as loads to the beam nodes, and displacements calculated for the thermal nodes. If no direct link between the thermal and structural meshes is available, displacements and temperatures could be interpolated for load transfer which adds to the

complexity of the solution. With or without a direct link, this method is still computationally taxing due to the need for a large thermal mesh.

The last option would be to simplify the temperature profile of the cross section. Thornton presents such a method, where the temperature profile is simplified to an average temperature and a perturbation temperature [9]. This method is ideal for modeling thermal snap of the HPSA because it drastically reduces the thermal nodal count and can be used with the structural beam elements. This method for simplifying the temperature profile will be presented further in the following section.

3.2. Simplification of the Temperature Profile

A tube under a unidirectional radiant heat source, like seen in Figure 7, exhibits a temperature distribution which varies along its surface. This temperature profile is dependent upon material, optical, and geometrical properties of the cross section along with the heat flux being applied. Internal and external radiation makes the problem nonlinear since the heat exchange from surface to surface and surface to space are dependent upon temperatures to the fourth power, as shown in the equation below.

$$Q_{12}=A_1 v_{12} \epsilon \sigma \left(T_2^4-T_1^4\right) \tag{11}$$

where $Q_{12}$is the heat transfer due to radiation, $A_1$is the surface area of object one, v_{12} is the view factor between object one and two, ϵ is the emissivity associated with object one's surface, σ is the Stefan Boltzmann constant, and T_1 and T_2 are the temperatures of object one and two respectively.

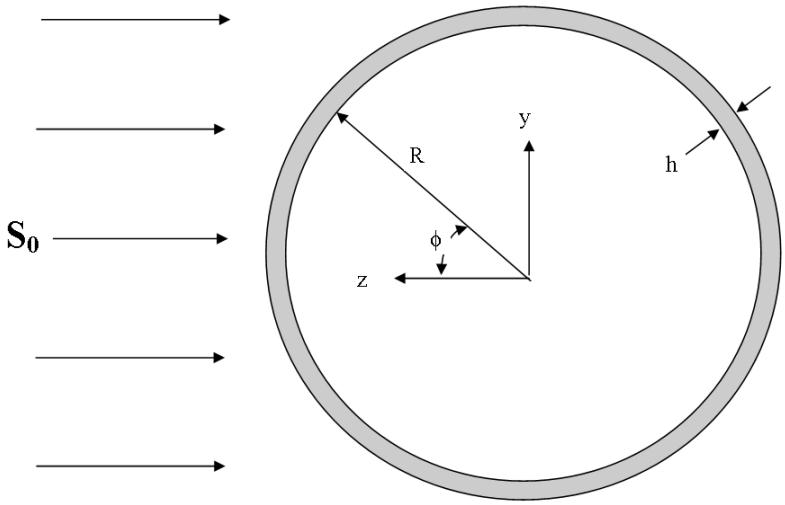

Figure 7. Diagram of STEM cross section with heat flux applied

Conservation of energy provides an equation for temperature of a tube as a function of position along the length of the beam x, angular position along the circumference ϕ, and time t:

$$\frac{d}{dt}T(x,\phi,t) - \frac{k\frac{d^2}{d\phi^2}T(x,\phi,t)}{\rho c R^2} + \frac{\phi\sigma T(x,\phi,t)^4}{\rho c h} = \frac{\alpha S \delta \cos(\phi)}{\rho c h} \tag{12}$$

Where k,ρ,c,R,h,α,S, and δ are conductivity, density, capacitance, radius of the beam, the wall thickness, absorptivity, solar heat flux input, and a function to show that only heat fluxes will applied to one side of the tube. The input solar heat flux is dependent on the magnitude of the S_0 the angle of incoming heat flux θ and the slope of the tube $\frac{d}{dx}w_b(x)$.

$$S=S_0 \cos\left(\theta-\frac{d}{dx}w_b(x)\right) \tag{13}$$

The distribution of the heat flux along the circumference can be represented by the following Fourier series expansion which neglects higher order terms.

$$\delta\cos(\phi)=\frac{1}{\pi}+\frac{1}{2}\cos(\phi) \tag{14}$$

Substitution of (13) and (14) into (12) yields the following.

$$\frac{d}{dt}T(x,\phi,t)-\frac{k\frac{d^2}{d\phi^2}T(x,\phi,t)}{\rho cR^2}+\frac{\phi\sigma T(x,\phi,t)^4}{\rho ch} = \frac{\alpha S_0\cos\left(\theta-\frac{d}{dx}w_b(x)\right)\left(\frac{1}{\pi}+\frac{1}{2}\cos(\phi)\right)}{\rho ch} \tag{15}$$

Making the assumption that the temperature of the cross section is the sum of average temperature $T_{avg}(x,t)$ and a perturbation temperature $T_m(x,t)$ which varies along the face,

$$T(x,\phi,t)=T_{avg}(x,t)+T_m(x,t)\cos(\phi) \tag{16}$$

and that the magnitude of the perturbation temperature is much smaller than the average temperature,

$$T_m<T_{avg} \tag{17}$$

the perturbation temperature becomes decoupled from the average temperature in (15) and provides two differential equations which can be solved for the temperature of the tube.

$$\frac{d}{dt}T_{avg}(x,t)+\frac{\sigma\epsilon T_{avg}(x,t)^4}{\rho ch}=\frac{\alpha S_0\cos\left(\theta-\frac{d}{dx}w_b(x)\right)}{\pi\rho ch} \tag{18}$$

$$\frac{d}{dt}T_m(x,t)+\left(\frac{k}{\rho cR^2}+\frac{4\sigma\epsilon T_{avg}^3}{\rho ch}\right)T_m(x,t)=\frac{\alpha S_0\cos\left(\theta-\frac{d}{dx}w_b(x)\right)}{2\rho ch} \tag{19}$$

Assuming that the average temperature left in (19) is the steady state average temperature, the time constant becomes

$$\tau=\left(\frac{k}{\rho cR^2}+\frac{4\sigma\epsilon T_{avg,ss}^3}{\rho ch}\right)^{-1} \tag{20}$$

Substituting back into (19) we get the following equation

$$\frac{d}{dt}T_m(x,t)+\frac{T_m(x,t)}{\tau}=\frac{\alpha S_0\cos\left(\theta-\frac{d}{dx}w_b(x)\right)}{2\rho ch} \tag{21}$$

Inspection of (18) and (21) shows that the average temperature will be nonlinear with radiation included while the perturbation temperature remains linear. With the beam undeflected, the steady state average temperature and perturbation temperature are predicted to be

$$T_{avg,ss}=\left(\frac{\alpha S_0\cos(\theta)}{\pi\sigma\epsilon}\right)^{\frac{1}{4}} \tag{22}$$

$$T_{m,ss}=\frac{\alpha S_0\cos(\theta)\,\tau}{\rho ch} \tag{23}$$

The ideal method for incorporating these equations into an ANSYS model would be to represent an entire cross section of the beam as a single node. The average temperature would be modeled as a thermal mass element at this node which radiates to

a space node through the use of a radiation link element. The perturbation temperature can be represented by a one degree of freedom spring-damper element connected to a ground node. Loads can then be calculated for a given incident angle and beam rotation at each node for every time step and applied as updated nodal forces.

A 2D analysis of a STEM cross section was created to validate the simplified temperature profile method. The analysis is explained further in the section that follows.

3.3. Full Thermal Model vs. the Simplified Thermal Model

The 2D thermal analysis of the STEM cross section was created in ANSYS. The mesh was generated in the XY plane. The cross section was represented by four node 2D thermal solid elements.

The model includes both internal and external radiation. Internal radiation is solved using the ANSYS Radiosity Solver which calculates view factors for flagged surfaces of each element [10]. This method models the radiation as a radiosity vector which is iteratively solved for. The radiosity vector is then added to the force vector of the conduction problem to iteratively solve for temperatures.

External radiation is modeled using radiation surface elements because no view factors needed to be calculated; the exterior elements radiate to space and view factors are known to equal one. The space temperature is represented by a single node with a defined temperature near absolute zero (0.1 °K). These elements model radiation through the use of an equivalent conductivity which is updated as element temperatures change. This method of radiation tends to converge and solve faster than the radiosity method, but requires the view factors to already be known.

The solar heat flux is applied in a cosine fashion across the top of the outer surface. With the cylinder centered at (0,0), the heat flux can be represented by the equations below.

$$q(y)=\alpha S_0 * \frac{y}{R} \qquad 0<y<R, \tag{24}$$

Two analyses were performed, a steady state analysis and time transient analysis over 4000 seconds. Results for the two analyses are provided in the sections that follow. The parameters used for both analyses can be seen in Table 2.

Table 2. Parameters used in thermal steady state and thermal transient analyses

Parameter	Value	Unit	Description
R	1.058E-02	m	radius
h	2.35E-04	m	thickness
ε_i	0.13		inner emissivity
ε_o	0.13		outer emissivity
α_o	0.50		outer absorptivity
k	16.61	W/m-K	thermal conductivity
q_s	1.350E+03	W/m^2	solar heat flux
Ts	0.1	°K	temperature of space
ρ	7.01E+03	kg/m3	density
c	5.02E+02	J/kg-K	specific heat
T_i	189.59	°K	initial temperature
σ	5.67E-08		Stefan-Boltzmann constant
t_f	4000	s	final time
Δt	8	s	time step

3.3.1. Thermal Steady State Analysis of the STEM Profile

The solution provides temperatures for a cross section of the STEM. Figure 8 shows a contour plot of the temperature distribution at steady state. A comparison of the steady state temperature distributions between the full cross section model and the first order approximation can be seen in Figure 9. The temperature distributions visually match up well, and the normalized root mean square error between the full model and 1st order approximation temperature distributions is only 4.66%. The steady state temperature difference between top and bottom for the analysis is 17.11°K while the approximation predicts 18.26°K, 6.72% greater than the full model. Therefore, the approximation will provide conservative results if used in the coupled transient analysis.

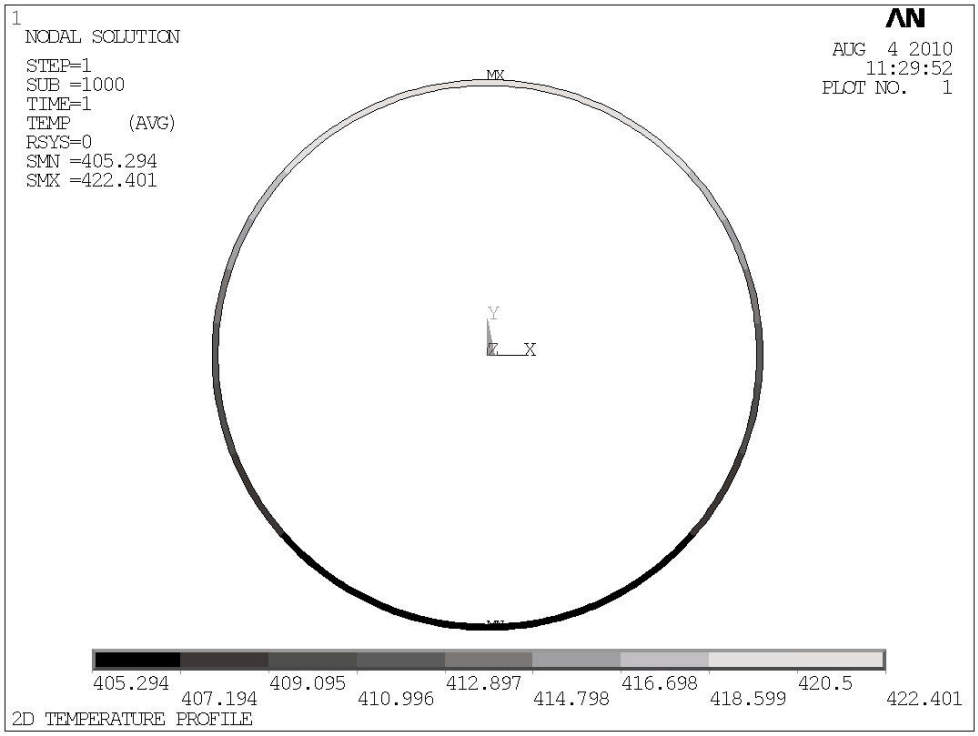

Figure 8. Steady state temperature profile for the STEM

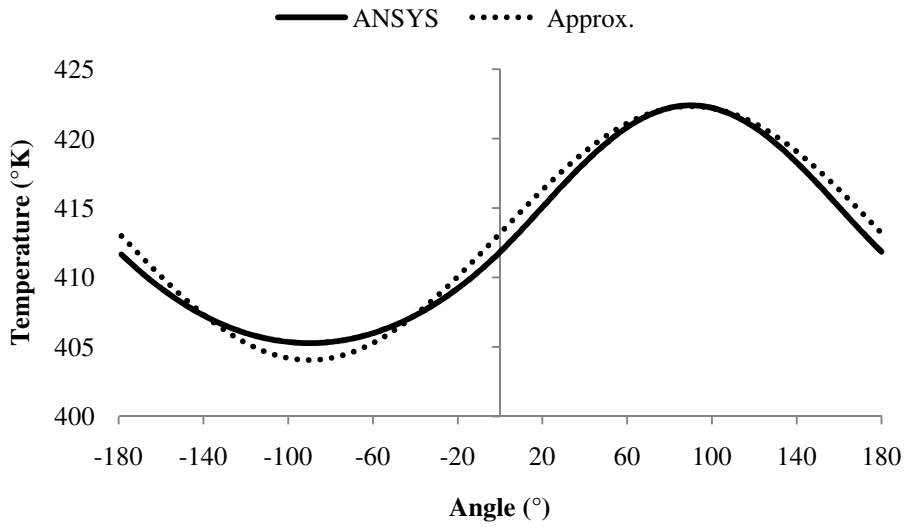

Figure 9. Comparison of the FEA steady state temperature distribution compared to the 1st order approximated solution

3.3.2. Thermal Transient Analysis of the STEM Profile

The transient analysis is evaluated for 4000 seconds allowing the cross section to approach steady state. Figure 10 shows the transient temperatures for the top and bottom of the full cross section model along with the average temperature from the simplified model. The approximate average temperature remains centered between top and bottom temperatures throughout the transient which is to be expected. The average temperature approximation accurately models the lump response of the system. The time history shows that the average temperature is within 1% its steady state value in 1992 (approximately 2000) seconds.

The temperature difference between the top and bottom temperatures measured by the full thermal model is plotted against the first order approximation in Figure 11. The temperature difference history shows that the 1st order approximation follows the full model closely for the first 500 seconds where most of the thermal excitation of the STEM is expected to occur. Thereafter, the nonlinearities in the full model become more drastic and result in the 6.72% error shown by the steady state thermal analysis.

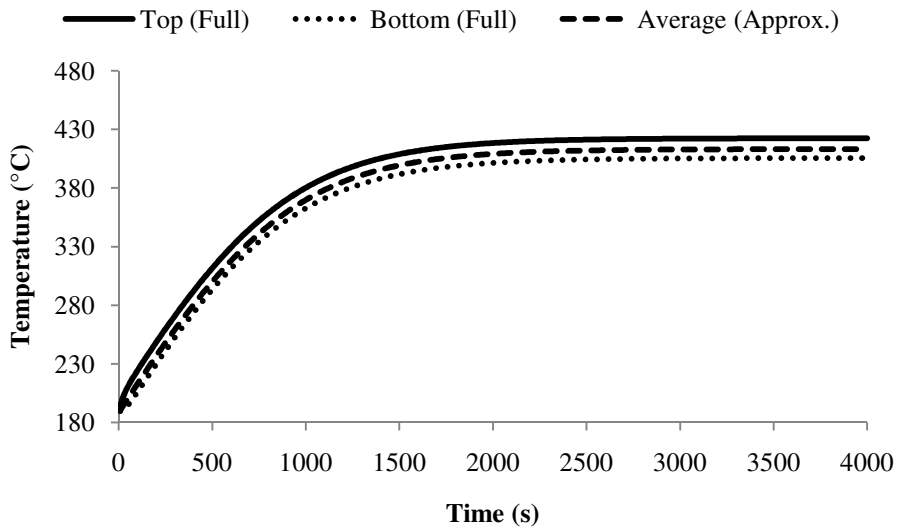

Figure 10. Transient temperatures for the top and bottom of the Bow Beam predicted by ANSYS

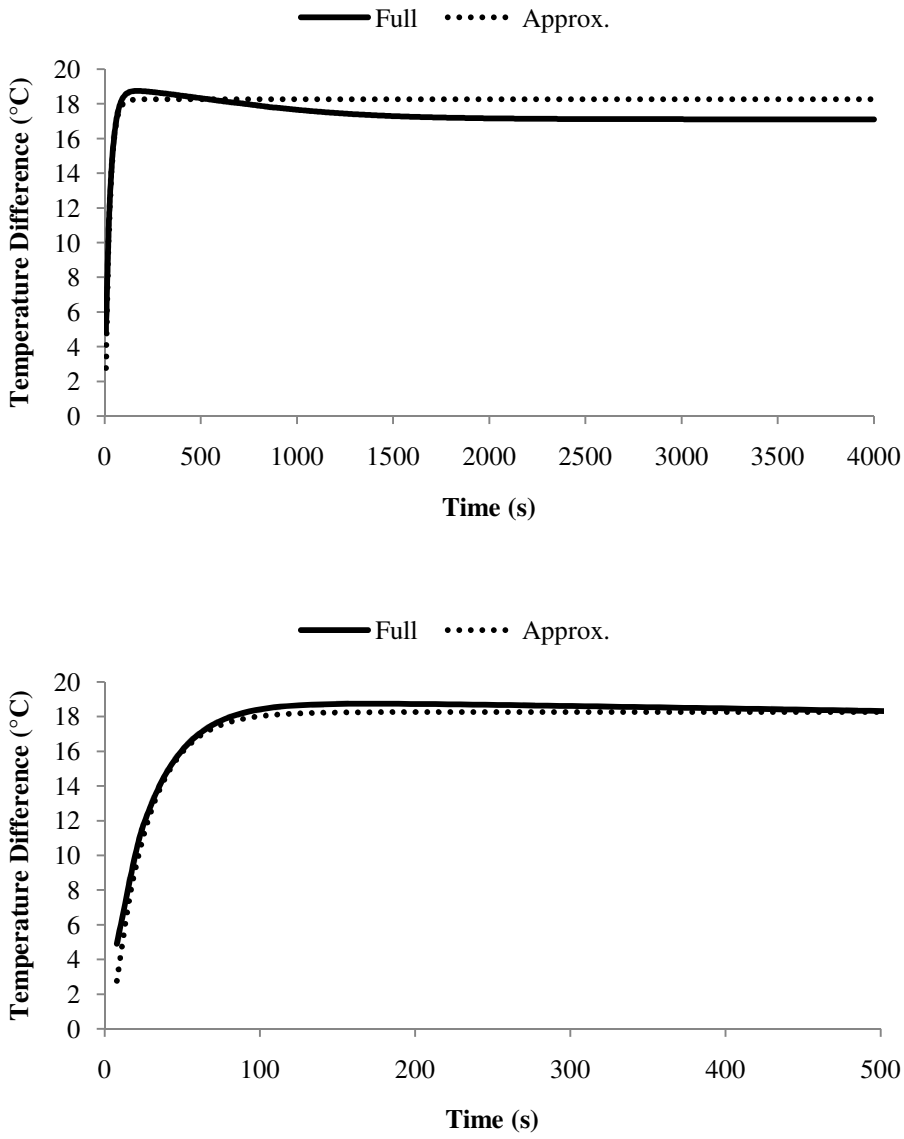

Figure 11. Comparison of the transient temperature difference for the full model and 1st order approximation model over 4000 seconds (top) and 500 seconds (bottom)

3.4. Model Comparison

The full model has 556 degrees of freedom while the simplified model has only 2. The time needed to solve the 4000 second transient analysis for the full and simplified models were respectively 36.7 sec and 5.5 sec. Therefore the simplified model solved 85% faster than the full model. Time savings were expected to be much more due to the drastic reduction in degrees of freedom which was 99.64%.

Although not certain, it's expected that solution times were limited by an internal process of ANSYS such as time needed to open and close files with every time step. Everything else, such as equation solving and file reading and writing, would be directly related to the number of degrees of freedom. If these intermediate processes are comparable to the time needed to solve a given time step, then the time savings will be reduced. However when multiple cross sections along the beam need to be modeled, these time savings are expected to increase because the intermediate steps become relatively smaller. Therefore when the temperature distribution needs to be found over multiple locations in a solar wing transient analysis, the time savings will be more noticeable.

3.5. Summary

- Model complexity and processing time for the thermal model of the STEM can be substantially reduced by representing the temperature distribution along the profile as the sum of an average temperature and perturbation temperature.
- The simplified model provides conservative results for the temperature gradient across the STEM cross section.
- Perturbation temperatures reach steady state in approximately 500 seconds while average temperatures are in about 2000 seconds.

4. UNDER UNIDIRECTIONAL SOLAR RADIANT HEAT

4.1. Single Solar Wing Considerations

Coupled thermal structural simulations are performed with a finite element (FE) analysis. The FE analysis can provides an unbiased means of comparison between the responses of different wing assemblies. The wings being considered are the HPSA Configuration 2 (HPSA2), and HPSA Configuration 3 (HPSA3), Hubble Space Telescope (HST), HPSA Straight STEM Equivalent (SSE). The Hubble response provides a baseline for what type of response previous wing designs encounter. The Straight STEM Equivalent demonstrates how a solar wing the size of HPSA reacts without the aid of tethers or STEM bowing. HPSA Configuration 2 and 3 are the top design picks presented by Stribling [2]. The objective is to prove that one of these HPSA designs will reduce the effects of thermal excitation on the wing in comparison to its straight wing counterparts, the Hubble and the Straight STEM Equivalent.

Performance is evaluated by the structural response of a 2D model for each single solar wing. By assuming symmetry down the center of the sheet width, each model includes half of a solar sheet, half of a spreader bar, and one STEM. For each HPSA configuration, two tethers are included and the STEM is bowed.

4.2. Model Description

The structural model for HPSA will include beam elements for the Bow STEM, structural link elements for the tethers and solar panel, and a structural mass for the

spreader bar. The STEM, tethers, and spreader bars will share a node at the tip of the wing. Tethers will have fixed translations where they fasten to the tether beams. The root of the STEM will have fixed translations and a rotation fixed at the root angle found in (4). The solar panel will have a fixed translation in the y and a force equal to half of the panel tension applied at the panel-spool interface location. For the straight STEM model, tether stiffnesses will be deactivated by the use of a stiffness matrix multiplier equal to 1e-6 by default in ANSYS, and the root angle will be set to zero.

Damping for the structural field transient analysis will be applied through the use of a stiffness matrix multiplier. This method creates a damping matrix by multiplying the stiffness matrix by a specified constant, β. This term can be calculated for a desired damping ratio and frequency using the following equation:

$$\beta = \frac{2\zeta}{\omega} \tag{25}$$

where ζ is the damping ratio and ω is the frequency in rad/s. This method, also known as proportional damping, can be used when exact damping properties of a structure are unknown. Often a minimum damping ratio is used for common structures and the frequency is selected to be the dominant modal frequency. In the case of the solar wing, this would be the first natural frequency which includes bending of the STEM.

The thermal model will be made up of conductive link elements to represent the STEM, and thermal masses to represent each of the tethers. With the length to diameter ratio being so large and radiation being dominant, the temperature gradient along the tether is negligible and can therefore be modeled with a thermal mass. Radiation links will be used to model external radiation from the beam and tethers to space. Spring-

damper elements with a connection to ground will be used to model the cross sectional perturbation temperature at every STEM node.

Structural boundary conditions: (26)

General

Solar Panel Spool: $u_y=0$, $f_x=\frac{1}{2}P_{sp}$

Hubble and Straight STEM Equivalent

STEM Root: $u_x=0$, $u_y=0$, $\theta_z=0$

HPSA Configuration 2 and 3

Tether Tips: $u_x=0$, $u_y=0$

STEM Root: $u_x=L_{arc}-L_c$, $u_y=0$, $\theta_z=\theta_{root}$

Parameters

4.3. Solution Algorithm

Two popular techniques used in solving coupled problems with finite elements include the direct method and the indirect method. Direct coupling uses specially formulated coupled-field elements which contain all necessary degrees of freedom, and coupling is included in the physics of the element either through matrices or element load vectors. Therefore, a coupled problem can be solved in a single analysis because coupling is handled internally. The indirect, or load transfer method, requires that the separate analyses be performed and results from one analysis applied as loads in another analysis. With the indirect method, care must be taken in what loads are transferred and

how they are applied. As a result, the indirect method can be more user intensive. However, the indirect method can be performed between separate analyses and separate meshes and therefore can offer more flexibility to the user [11].

ANSYS does not currently provide a coupled-field thermal-structural beam element, so the indirect method will be used for the thermal snap simulation of the Bow STEM. The system problem is divided into three separate physics which will be solved individually in the following order: nonlinear structural, nonlinear thermal for average temperatures and linear thermal for perturbation temperatures. After each time step, the temperatures are updated for the structural analysis, and angles of incident are updated for the thermal. A flow chart of the solution algorithm can be seen in Figure 12. This process will be handled by using ANSYS's Multi-Field Solver (MFS) [11] which was specifically developed for solving coupled problems with the load transfer method.

In the load transfer method for a thermal-stress analysis, there is a two way interface between structural and thermal models; temperatures are provided to the structural model, and displacements supplied to the thermal model. The structural models often use the temperatures to update material properties and internal loadings due to thermal stress. The thermal model uses the displacements to update geometry dependent loading such as heat fluxes in the case of unidirectional radiant heating.

Thermal stress loads are modeled in ANSYS by applying temperature loads on beam elements. In a 2D beam, ANSYS requires a top and bottom temperature for each end node of the beam element as seen in Figure 13. These four temperatures are applied as element body force loads and are provided by (27).

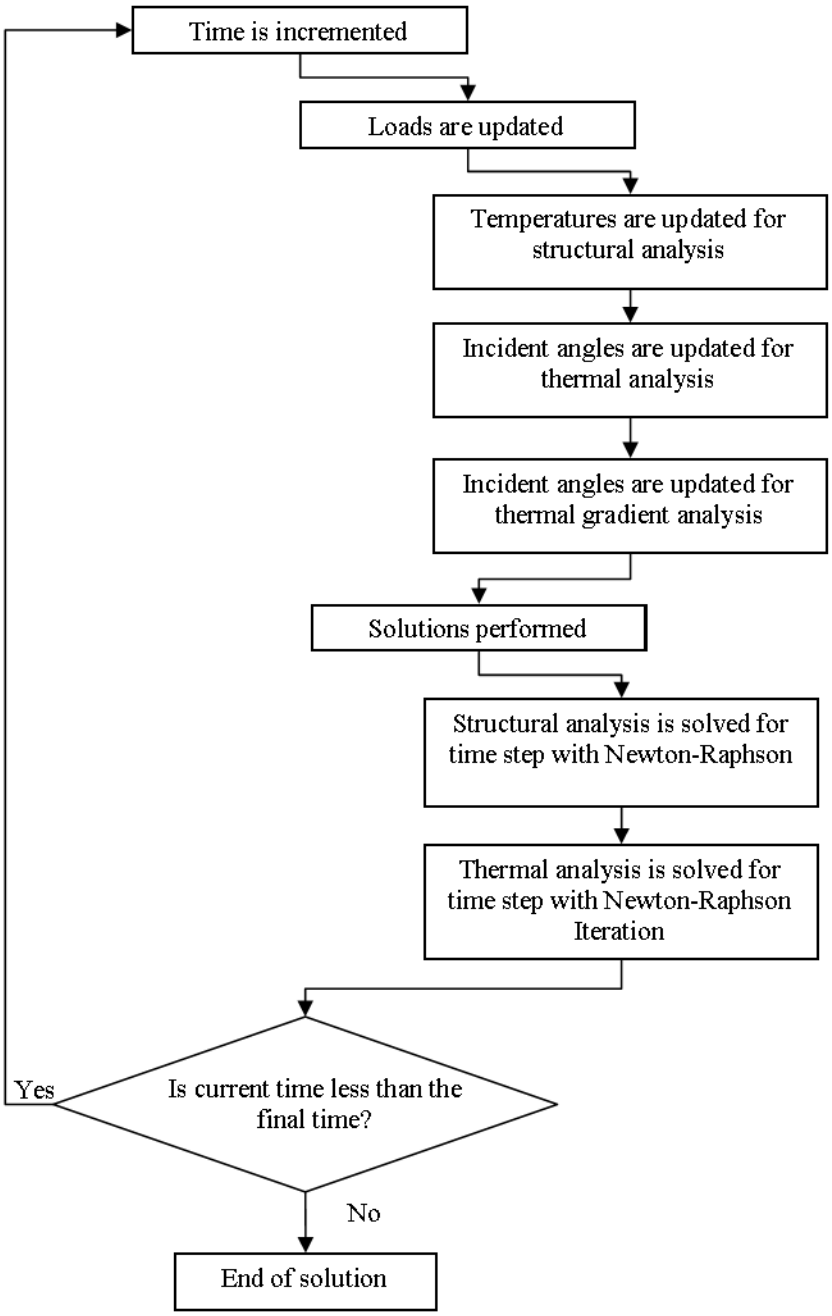

Figure 12. Flow chart for the multiple physics solution algorithm

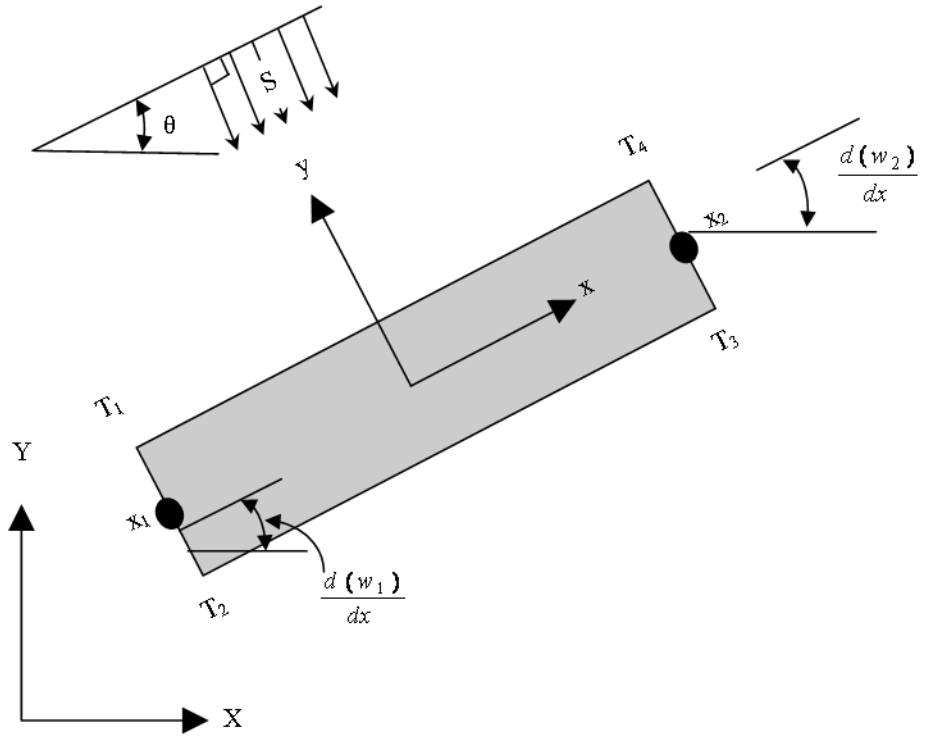

Figure 13. Diagram of temperature loads for a 2D beam in ANSYS.

$$T_1=T_{avg}(x_1,t)+T_m(x_1,t) \quad (27)$$
$$T_2=T_{avg}(x_1,t)-T_m(x_1,t)$$
$$T_3=T_{avg}(x_2,t)-T_m(x_2,t)$$
$$T_4=T_{avg}(x_2,t)+T_m(x_2,t)$$

Heat fluxes from the sun will be applied to each temperature degree of freedom, T_{avg} and T_m, as a nodal heat input. Amplitude of the heat will be calculated as follows for the average temperature degree of freedom:

$$Q_{avg}=\alpha q_s R L_e \left|\cos\left(\theta-\frac{d}{dx}w_b\right)\right| \tag{28}$$

where L_e is the length of an element. The absolute value of the incident angle multiplier $\cos\left(\theta-\frac{d}{dx}w_b\right)$ is included under the assumption that the radiant heat flux will either hit top or bottom sides for all angles and will always be a positive heat input. However for the perturbation temperature heat input, the sign indicates which side the heat is coming from and can have both positive and negative values. Therefore, the heat input for the gradient degree of freedom is

$$Q_m=\frac{\alpha q_s}{2\rho c h}\cos\left(\theta-\frac{d}{dx}w_b\right) \tag{29}$$

It should be noted that conduction along the length of the beam is included in the average temperature model, and therefore its nodal heating is proportional to the size of the thermal link elements. However, the perturbation temperatures are completely uncoupled from one another and are therefore not dependent on the size of the element.

4.4. Validation of Algorithm

Thornton [9] has performed a coupled thermal-structural analysis of a Hubble Space Telescope (HST) solar wing and documented his results. A similar HST model was created in ANSYS to reproduce Thornton's results and validate the indirect coupled solution method which will be used for evaluating the HPSA design later in this paper.

Three transient cases were performed with the indirect coupled model in ANSYS with variations in damping and angle of incidents for the solar heat flux. Tip deflections

of the wing were plotted for each case along with Thornton's results and can be seen in Figure 14, Figure 15, and Figure 16. The indirect coupled ANSYS model follows Thornton's model nicely. Both quasi-static curve and superimposed oscillations of the ANSYS model are closely adjacent to Thornton's curves. Therefore the indirect coupled method described earlier is fully capable of modeling the thermally induced bending vibrations of flexible solar array.

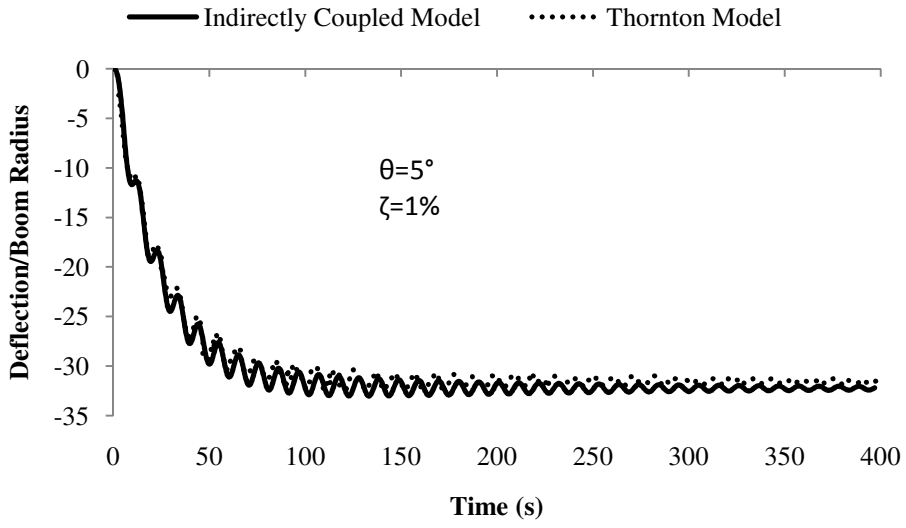

Figure 14. Stable HST tip deflection

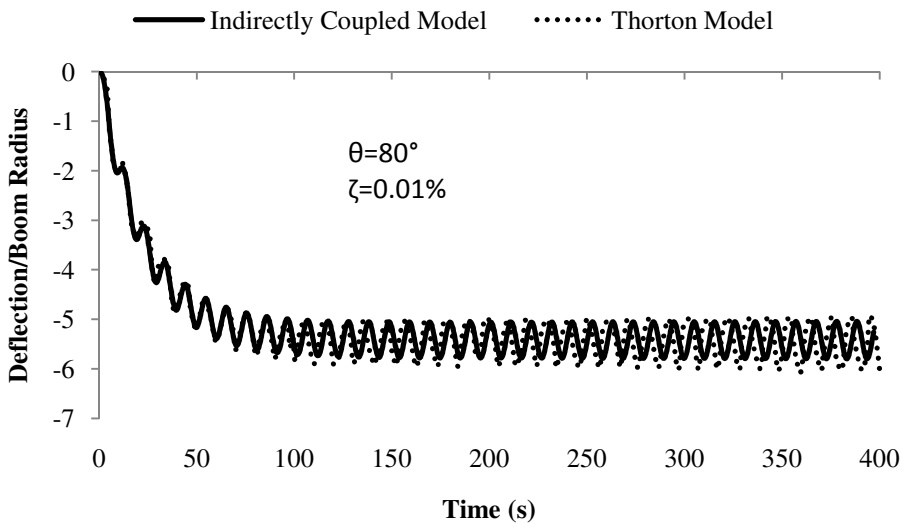

Figure 15. Unstable HST tip deflection

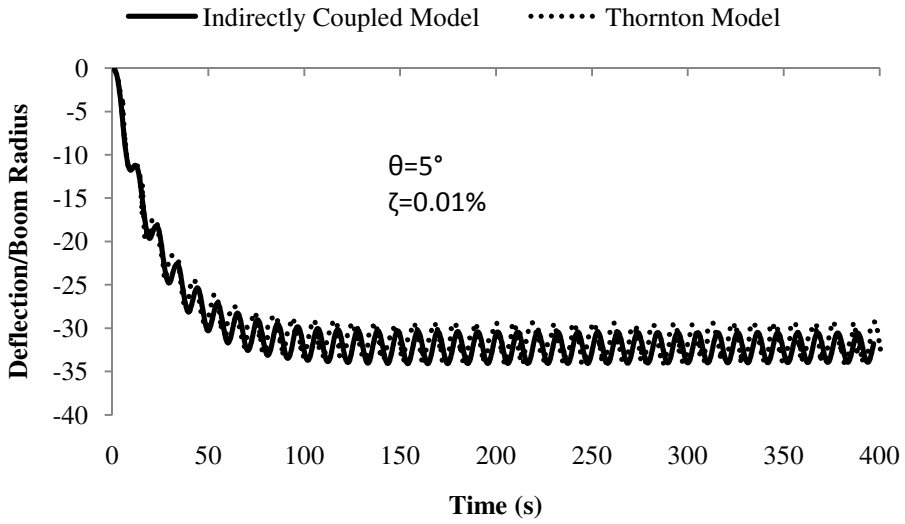

Figure 16. Marginally stable HST tip deflection

4.5. Parameters and Assumptions

A full list of parameters used for each wing configuration is provided below in Table 3. Boeing did not identify every parameter necessary for a complete transient analysis, so assumptions are made to account for these parameters [2]. The sections that follow describe those assumptions.

Table 3. List of parameters used in wing simulations

Parameter	Description	Units	HST	SSE	HPSA 2	HPSA 3
A	STEM cross sectional area	m^2	1.61E-05	1.54E-05	1.54E-05	1.54E-05
A_t	tether area	m^2	0	0	2.28E-07	2.28E-07
b	half spreader bar width	m	1.428	1.943	1.943	1.943
b'	half solar blanket width	m	1.194	1.791	1.791	1.791
c_b	STEM specific heat	J/kg-K	502	502	502	502
c_t	tether specific heat	J/kg-K	0	0	340	340
D_t	tether diameter	m	0	0	7.50E-04	7.50E-04
E_0	Earth heat flux	W/m^2	1350	1350	1350	1350
E_b	beam modulus of elasticity	N/m^2	1.93E+11	1.93E+11	1.93E+11	1.93E+11
E_{sb}	solar blanket modulus of elasticity	N/m^2	2.60E+09	2.60E+09	2.60E+09	2.60E+09
E_t	tether modulus of elasticity	N/m2	0	0	7.03E+10	7.03E+10
f_b	tip frequency	Hz	0.097	0.033	0.545	0.809
h_b	thickness	m	2.35E-04	2.35E-04	2.35E-04	2.35E-04
H_c	cord height	m	0	0	1.52	1.52
H_i	initial cord height	m	0	0	2.54E-03	2.54E-03
H_m	module height	m	0	0	3.20	4.65
I_b	area moment of inertia	m^4	8.865E-10	8.448E-10	8.448E-10	8.448E-10
kb	thermal conductivity	W/m-K	16.61	16.61	16.61	16.61
k_t	tether conductivity	W/m-K	0	0	0.04	0.04
L_{arc}	arc length	m	5.91	15.24	15.61	15.61
L_c	cord length	m	5.91	15.24	15.24	15.24
Ms	spreader bar mass	kg	1.734	2.359	2.359	2.359
P_b	STEM compressive load	N	14.75	5.37E-01	6.67	6.67
P_{sb}	half solar blanket tension	N	14.75	5.37E-01	4.45	4.45

Table 3. Continued

Parameter	Description	Units	HST	SSE	HPSA 2	HPSA 3
R_b	radius	m	1.092E-02	1.058E-02	1.058E-02	1.058E-02
S_0	solar heat flux	W/m^2	1350	1350	1350	1350
α_b	STEM absorptivity		0.5	0.5	0.5	0.5
$\alpha_{CTE,b}$	STEM coefficient of thermal expansion	m/m-K	1.69E-05	1.69E-05	1.69E-05	1.69E-05
$\alpha_{CTE,t}$	tether coefficient of thermal expansion	m/m-K	0	0	-2.00E-06	-2.00E-06
α_t	tether absorptivity		0	0	1	1
ε_b	STEM emissivity		0.13	0.13	0.13	0.13
ε_t	tether emissivity		0	0	0.76	0.76
$\eta_{xv,b}$	beam Poisson's ratio		0.30	0.30	0.30	0.30
θ_{root}	STEM root angle	rad	0	0	0.308	0.308
ρ_b	STEM density	kg/m^3	7.01E+03	7.01E+03	7.01E+03	7.01E+03
ρ_{sb}	solar blanket density	kg/m^3	1420	1420	1420	1420
ρ_t	tether density	kg/m^3	0	0	1440	1440
σ	Stefan-Boltzmann constant	$W/m2-K^4$	5.67E-08	5.67E-08	5.67E-08	5.67E-08
σ_{sb}	mass per unit area	kg/m^2	1.589	0.120	0.120	0.120

4.5.1. Spreader Bar Mass

The HPSA design calls for an End Beam, or Spreader Bar, but a mass for the bar is not specified. However, the length of the bar is known to be 1.943 m (12.75 ft). Assuming that the bar has the same weight to length ratio as Hubble's spreader bar, a Spreader Bar mass can be found.

$$M_{s,HPSA}=M_{s,HST}*\left(\frac{b_{HPSA}}{b_{HST}}\right) \tag{30}$$

where M_s specifies the spreader bar mass, b represents half the spreader bar width, and the subscripts HPSA and HST deviates between HPSA and Hubble parameters. Substituting values into (30),

$$M_{s,HPSA} = (1.734\ kg) * \left(\frac{1.943\ m}{1.428\ m}\right) = 2.359\ kg \tag{31}$$

the spreader bar mass for HPSA is found to be 2.359 kg.

4.5.2. Panel Tension for Straight STEM Equivalent

The HPSA design states that a 2.0 lb panel tension is to be utilized. This is higher than the Straight STEM Equivalents buckling load. Hubble's design called for a panel tension which was 31% of the buckling load. This factor will be used to specify the panel tension for the Straight STEM Equivalent model. Utilizing the Euler buckling load equation (1), substituting in values for the HPSA STEM, and utilizing the fixed-free effective length (K=1),

$$P_{cr} = \frac{\pi^2 \left(1.93e11 \frac{N}{m^2}\right)(8.448e\text{-}10 m^4)}{\left((2)(15.24m)\right)^2} = 1.73\ N \tag{32}$$

the buckling load is found to be 1.73 N. Multiplying by the 31% load factor, the panel tension is found to be 0.537 N.

4.5.1. Tether Properties

No material or dimensions were specified for the tethers. Research shows that tethers have been utilized in many space related projects ranging from momentum exchange to electromagnetic power generation. The most likely candidate for the tethers to be used on HPSA will be those similar to those from previous space missions. One such project in particular, the Small Expendable Deployer System SEDS [12], demonstrated how tethers could be used to deorbit a payload. The SEDS tether was able to withstand a tension of over 43 N, much higher than those being expected by HPSA.

However, it's expected that the tether diameter was selected for micrometeoroid survivability rather than load capacity. With HPSA being expected to encounter similar orbits, a tether similar to the SEDS-I is justified for this analysis.

SEDS-I tethers were made up of hollow braided Kevlar, so the area of the cord cannot be calculated by using the area of a circle. Instead, the area can be found from the known tether length (20 km) and mass (6.7 kg) and the tether density (1440 kg) [12]. The assumed material properties for Kevlar are listed in Table 4. Using the following equation,

$$A=\frac{LM}{\rho}=\frac{(20\text{ km})(6.7\text{ kg})}{(1440\text{ kg})}=2.28\text{e-}7\text{ m}^2 \tag{33}$$

where L is the length, M is the mass, and ρ is the density, the equivalent area is found to be 2.28e-7 m^2.

Table 4. Assumed Kevlar material properties

Property	Value	Units
Tensile Modulus[1]	7.03E+10	N/m^2
Density[1]	1440	kg/m^3
Specific Heat[1]	340	J/kg-°K
Thermal Conductivty[1]	0.04	W/m-°K
Coefficient of Thermal Expansion[2]	-2.00E-06	1/°K
Emissivity[3]	0.76	
Absorptivity[4]	1	

1. From Matweb ™ "Kevlar 29"[13]
2. From NASA "Space Tethers: Design Criteria"[14]
3. Lowest value for cloth found in "Heat Transfer: A Practical Approach"[15]
4. Assumed to maximize heat absorbed for conservative results.

4.5.2. Solar Panel Properties

Thornton's model only includes out of plane stiffness of the solar panel due to the tension. In order to model the solar panel in ANSYS, a 2D elastic element was selected for the model which includes both axial stiffness and the same transverse stiffness due to the panel tension. The element requires a density, modulus of elasticity, and area. For this reason, the sheet is assumed to be made of Kapton with properties shown in Table 5. An equivalent area for the sheet is calculated using the assumed density (ρ), half panel width (b'), and the mass to area ratio (σ_{sb}) which are provided for each design and is shown in (34).

$$A_{sb} = \frac{\rho b'}{\sigma_{sb}} \tag{34}$$

Table 5. Material properties from Matweb ™ for "DuPont™ Kapton® 50HN Polyimide Film, 13 Micron Thickness"[16]

Property	Value	Units
Tensile Modulus	2.60E+09	N/m^2
Density	1420	kg/m^3

5. RESULTS

Modal, static, and transient analyses were performed for the Hubble (HST), HPSA Straight STEM Equivalent (SSE), HPSA Configuration 2 (HPSA2), and HPSA Configuration 3 (HPSA3). Results for each model are presented in the following sections.

5.1. Modal Analysis

A prestressed modal analysis of the four solar wing configurations are performed in ANSYS. The first ten natural frequencies are presented in Table 6. Comparison of modal results for both HPSA configurations to the SSE shows a drastic 351% increase in the lowest natural frequency and a 52% increase when compared to HST. Therefore the addition of tethers along with bowing of the STEM significantly increases vertical stiffness of the wing tip. It should be noted that the first natural frequency of the Straight STEM configuration is very close to the 0.01 Hz minimal deployed frequency criteria specified by Stribling, while the lowest HPSA frequency is almost 15 times the minimal frequency [2].

A design frequency must be selected for the beta damping to be applied using (25). Given that the vibrations of the wing tip are the main concern of this study, the design frequency is set to the modal frequency which is expected to have the dominant response. In order to do so, transverse modal components at the tip node are compared between the mass orthonormalized mode shapes. The mode with the largest component is considered the most likely to be excited under the solar heat fluxes. The frequency

associated with this mode will be referred to as the tip frequency. The tip frequencies are highlighted in Table 6 and the coinciding mode shapes are presented in Figure 17. It should be noted that more than one frequency could be excited under the unidirectional solar radiant heating. However, the dominant mode to be excited is the main concern.

Table 6. First ten modes of each solar wing configuration

Mode	HST	SSE	HPSA 2	HPSA 3
1	0.097	0.033	0.147	0.148
2	0.323	0.064	0.294	0.297
3	0.546	0.110	0.437	0.446
4	0.773	0.160	0.545	0.595
5	1.005	0.212	0.630	0.731
6	1.243	0.266	0.769	0.809
7	1.488	0.320	0.923	0.928
8	1.738	0.376	1.081	1.081
9	1.996	0.426	1.155	1.176
10	2.260	0.439	1.252	1.256

*Modes with the highest tip deflections are highlighted

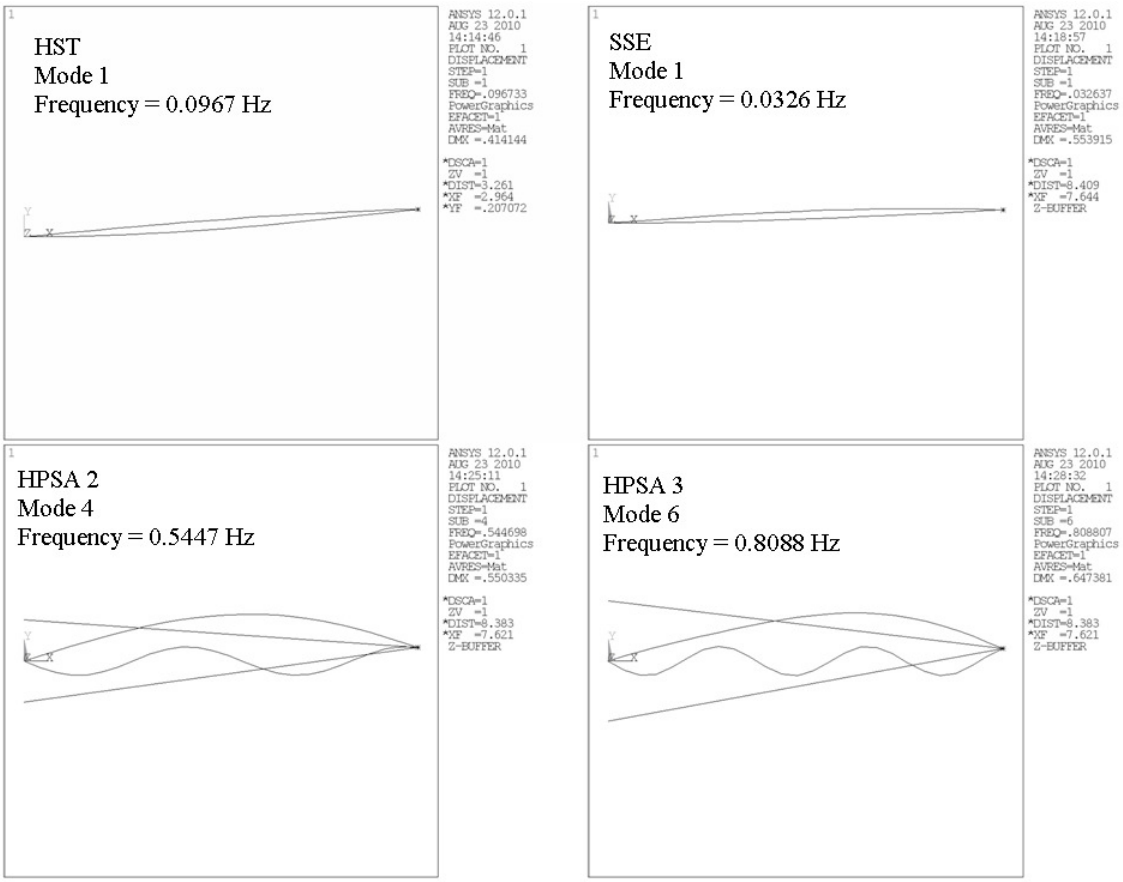

Figure 17. Mode shapes for each design with the largest tip deflection plotted in ANSYS.

To better understand each configuration's stability, the nondimensional frequencies are found for each design by multiplying each frequency by the thermal time constant in (20) where τ is 23.75 seconds for HST and 22.37 seconds for the remaining designs. The nondimensional frequencies are presented in Table 7. Ideally, the nondimensional frequencies should not be equal to 1, because more damping is required to maintain stability as this nondimensional frequency approaches one from both sides,

$-\infty$ and $+\infty$. Although the highlighted tip frequencies are most likely to be excited, comparison of the first natural modes alone still proves that HPSA2 and HPSA3 should be more stable than the HST and SSE. SSE has a nondimensional frequency relatively close to one which means more damping will be required for it to remain stable.

Table 7. First ten nondimensionalized modes of each solar wing configuration

Mode	HST	SSE	HPSA 2	HPSA 3
1	2.298	0.730	3.296	3.320
2	0.153	1.426	6.579	6.647
3	0.240	2.454	9.768	9.986
4	0.051	3.583	12.183	13.312
5	0.137	4.749	14.092	16.352
6	0.003	5.942	17.201	18.090
7	1.228	7.160	20.641	20.764
8	0.334	8.403	24.170	24.175
9	0.084	9.519	25.838	26.305
10	0.011	9.819	27.993	28.090

*Modes with the highest tip deflections are highlighted

5.2. Coupled Thermal-Structural Steady State Analysis

A steady state analysis is performed for each of the four wing configurations. The static analysis is similar to the transient method shown previously in Figure 12; however, transient effects are disabled in ANSYS, and multiple iterations are performed allowing the structure to reach its steady state deflected shape. The solar heat flux was applied at an incident angle of 0°.

Steady state transverse deflections along the beams of the models are plotted in Figure 18. Tip deflections for HST and the SSE are -0.36 m and -1.80 m respectively HPSA2 has its bottom tether go slack, and has a tip deflection of -0.61 m. Tethers for HPSA3 remain taut and has a tip deflection of only, -4.4 mm. Therefore in comparison with HST, HPSA3 can decrease tip deflections by 98.8%. However, HPSA3 does show an increase in cord height of 7.1% (0.12 m).

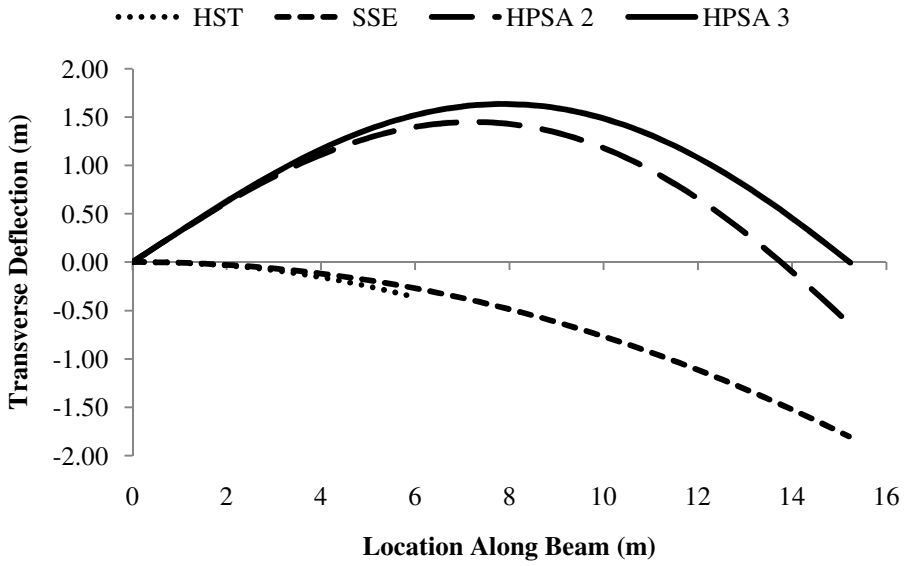

Figure 18. Steady state deflection in the Y along the straight STEM

Each configuration's temperatures, both average and perturbation, relate closely to their respective deflected shape with peak amplitudes occurring where the beam is normal to the heat source, a result of the cosine effect associated with the unidirectional Solar heating. Steady state average temperatures and perturbation temperatures are

shown in Figure 19 and Figure 20 respectively. Examining the plots of the perturbation temperatures, there is an offset between HST and SSE. This offset is due to the slight difference in radius between the two configurations, and its effect on the time constant in the perturbation equation, (21).

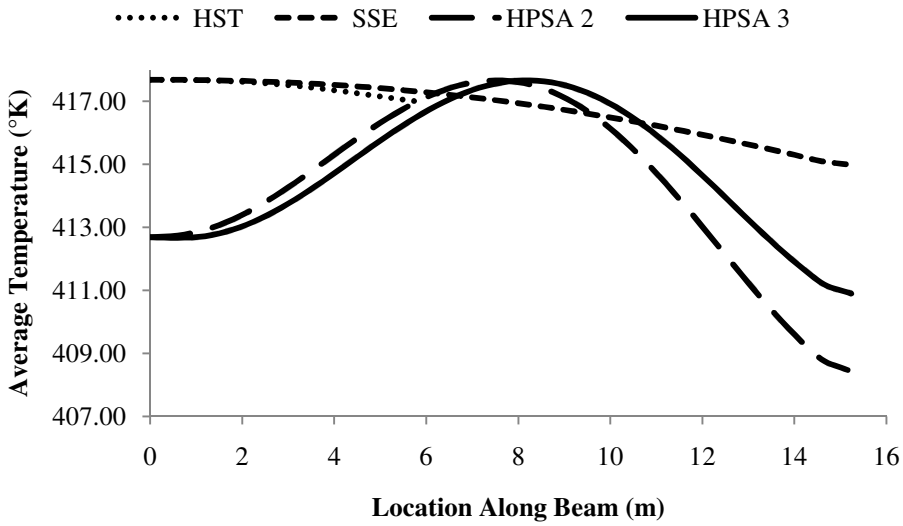

Figure 19. Steady state average temperatures along the length of the STEM

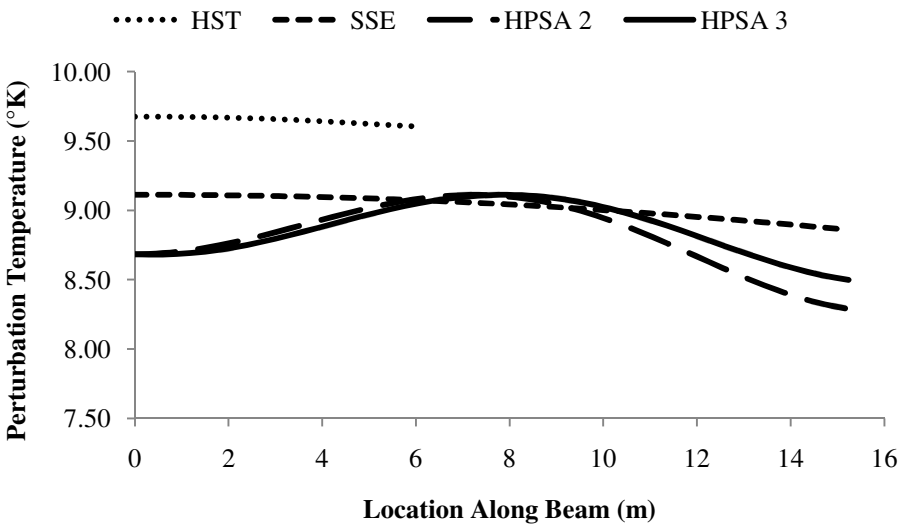

Figure 20. Steady state perturbation temperatures along the length of the STEM

5.3. Coupled Thermal-Structural Transient Analysis

The transient response of the STEM can be broken down into two components, a quasi-static motion and a superimposed oscillation. Of the two, the oscillation has the most significant effect on pointing accuracy. Quasi-static disturbances are easily accounted for by control systems while jittering due to oscillating disturbances are more difficult to filter out.

The transient response of the four wing configurations are examined and compared in the sections that follow. Each configuration will have two separate load cases performed with stepped unidirectional heating applied at 0° and 80° angles of incidence. A minimal value of beta damping ($\zeta = 0.01\%$) is applied at the tip frequency highlighted in section 5.1. This value is considered to be conservative based on the

range of values used by Thornton [9]. The transient will be evaluated for a 2000 second time range, the approximate time for the average temperature to reach 1% of its steady state value.

5.3.1. Hubble

Transient response of the Hubble solar wing can be seen in the following figures. Time history of the tip displacement is presented in Figure 21. The quasi-static component of the tip deflection is dominated by bending due to thermal gradient across the STEM cross section (or the perturbation temperature), and reaches steady state in approximately 100 seconds. Tip deflections go to approximately -35cm and -6cm for the 0° and 80° incident angles respectively. The 0° incident angle case is stable, but vibrations have not died out after 2000 seconds. The 80° incident angle has an unstable oscillation. Time history of the tip velocity shown in Figure 22 has similar behavior. A Fast Fourier Transform (FFT) analysis of the tip velocity histories presented in Figure 23 shows oscillations for both cases occurring at 0.096 Hz which is near the first natural frequency of HST (also the highest tip vibration mode).

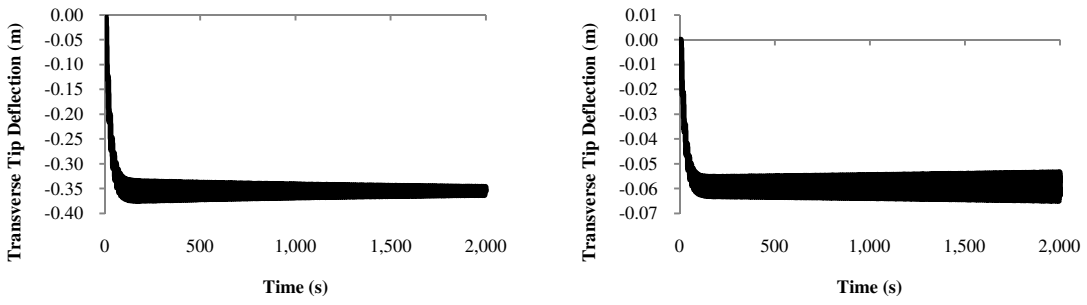

Figure 21. HST tip displacement histories for 0˚ (left) and 80˚ (right) incident angles

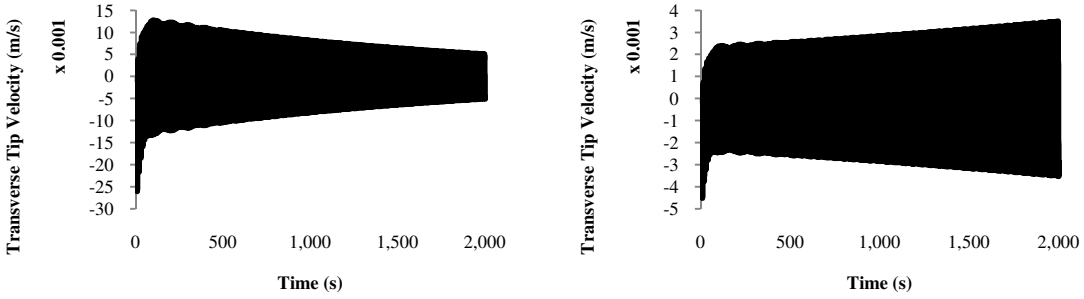

Figure 22. HST tip velocity histories for 0˚ (left) and 80˚ (right) incident angles

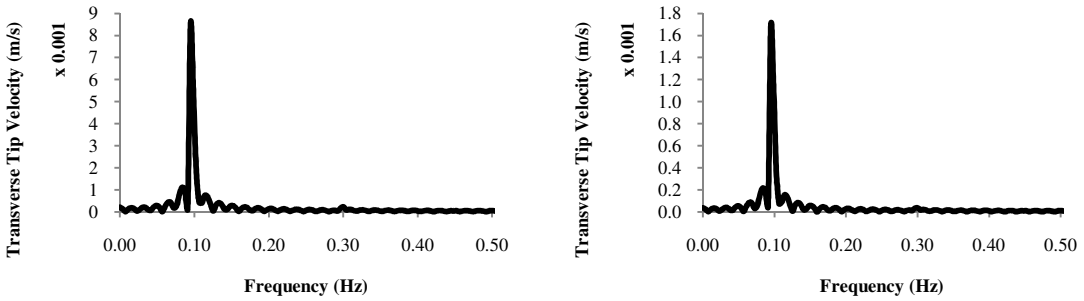

Figure 23. HST tip velocity FFTs for 0˚ (left) and 80˚ (right) incident angles

5.3.1. Straight STEM Equivalent

Transient results for the Straight STEM Equivalent to HPSA are shown in the figures that follow. SSE transverse tip deflection and velocity histories are shown in Figure 24 and Figure 25 respectively. Quasi-static tip deflections go to approximately -175cm and -27cm for the 0° and 80° incident angles correspondingly. Both incident angle cases are unstable. However, the 0° case has an oscillation which is growing much slower (1cm over 1000 seconds) than the 80° case (15cm over 1000 seconds). FFT of the tip velocities in Figure 26 show the first natural frequency of 0.033 Hz being excited

for both incident angle cases, and the 0° case also has components from the second natural frequency, 0.064 Hz.

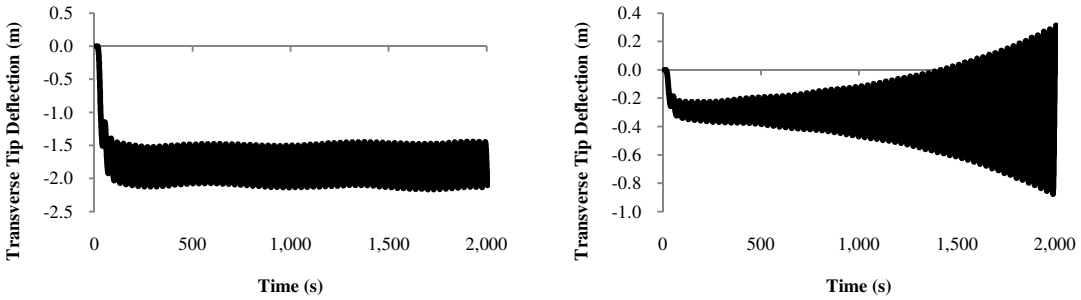

Figure 24. SSE tip displacement histories for 0˚ (left) and 80˚ (right) incident angles

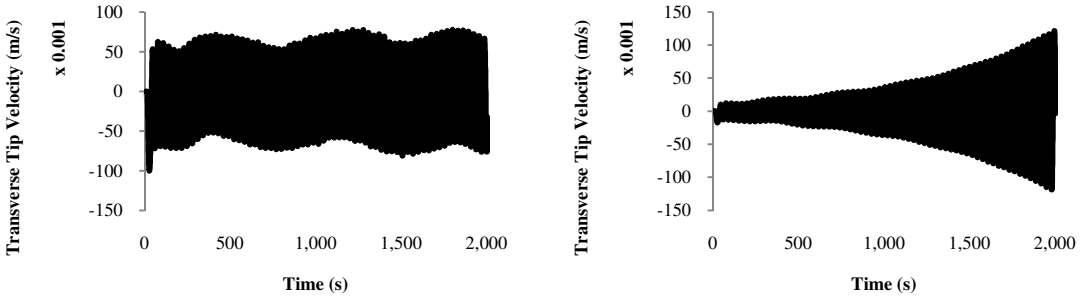

Figure 25. SSE tip velocity histories for 0˚ (left) and 80˚ (right) incident angles

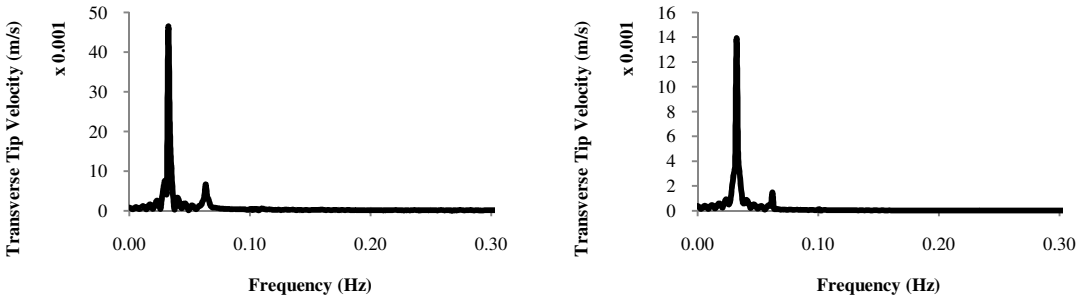

Figure 26. SSE tip velocity FFTs for 0˚ (left) and 80˚ (right) incident angles

5.3.2. HPSA Configuration 2

Transient responses for HPSA Configuration 2 are shown in the figures that follow with the tether tensions presented in Figure 27. Large changes in tension occur in the first 100 seconds and approach steady state in approximately 2000 seconds. Examination of the 0° incident angle case shows that Tether 2 (the lower tether) loses tension in 80 seconds while Tether 1 goes to 1.36 N. The sudden loss in Tether 2's tension leads to a marginally stable oscillation, while the 80° case maintains tension in both tethers throughout the transient and has steady state tensions of 1.81 N for Tether 1 and 0.78 N for Tether 2.

Tip deflections and velocities are presented in Figure 28 and Figure 29 correspondingly. The 0° case has a quasi-static deflection of -64cm and a marginally stable oscillation. The 80° case has an initial overshoot tip deflection of 11 mm at 30 seconds, a steady state deflection of 5 mm. The positive tip deflections are a result of

the cosine effect of the unidirectional heat flux applied at the obscure 80° incident angle on the bowed shape and also the tethers.

FFT plots of the HPSA2 tip velocity in Figure 30 show vibrations at 0.023 Hz for the 0° case which is lower than the first natural frequencies of both HPSA2 and SSE. The 80° case oscillates at multiple natural frequencies with the dominant being the 4th mode, 0.545 Hz, which is also recognized as the tip mode. The lower frequency in the 0° case is due the loss of tether tension which drastically reduces stiffness at the tip.

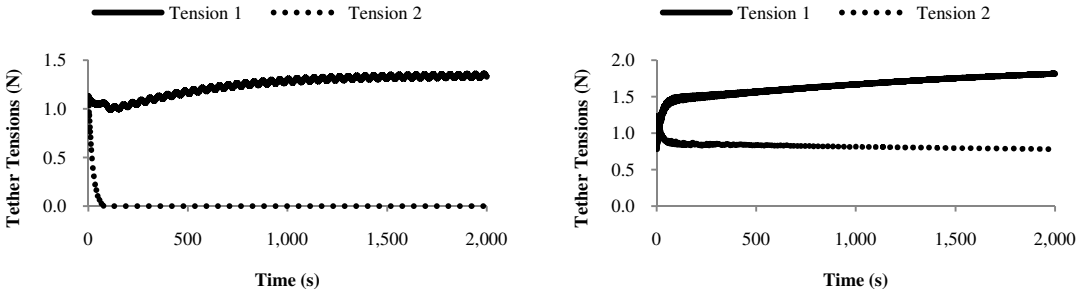

Figure 27. HPSA2 tether tension histories for 0˚ (left) and 80˚ (right) incident angles

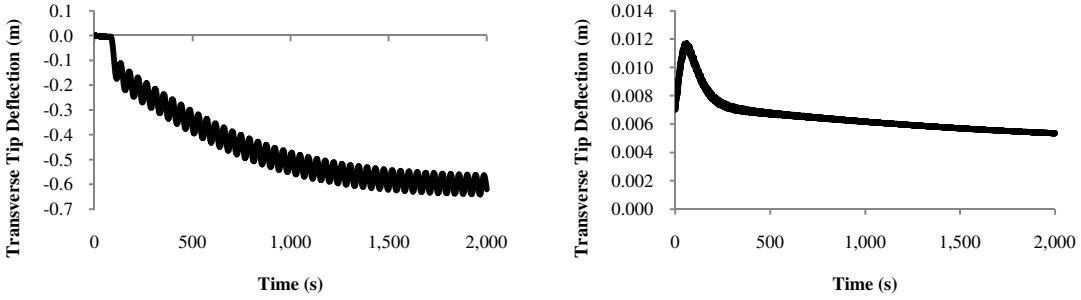

Figure 28. HPSA2 tip displacement histories for 0˚ (left) and 80˚ (right) incident angles

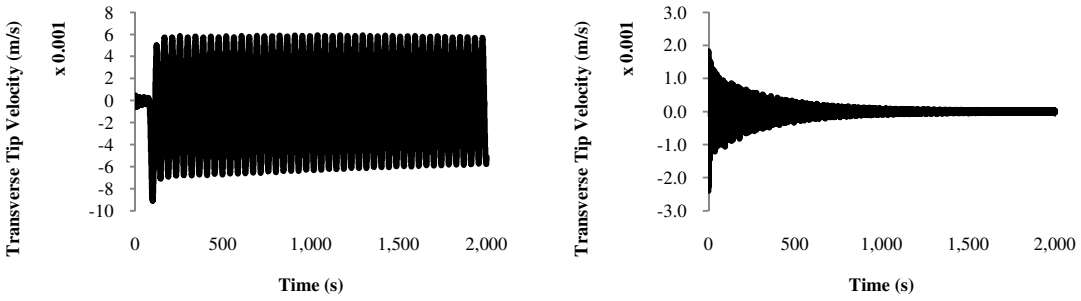

Figure 29. HPSA2 tip velocity histories for 0˚ (left) and 80˚ (right) incident angles

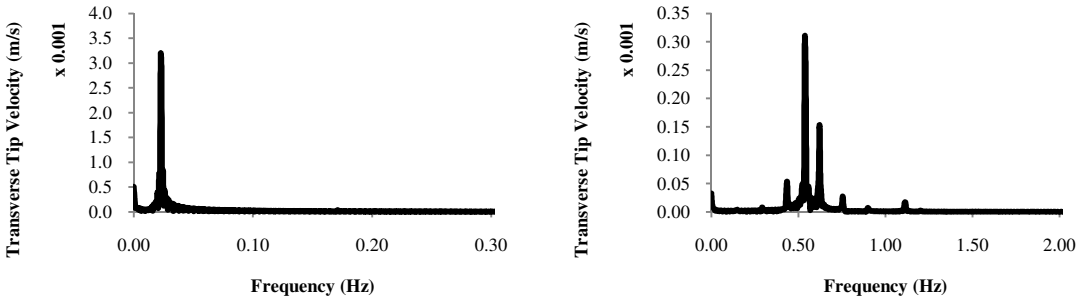

Figure 30. HPSA2 tip velocity FFTs for 0˚ (left) and 80˚ (right) incident angles

5.3.3. HPSA Configuration 3

Transient responses for HPSA Configuration 3 are presented in the following figures with tether tension histories shown in Figure 31. Tethers remain taut for both incident angle cases. The 0° case has steady state tensions of 1.52 N for Tether 1and 0.15 N for Tether 2 while the 80° case is 1.65 N and 0.95 N.

Transverse tip deflections and velocities are presented in Figure 32 and Figure 33 respectively. The 0° case has a steady state deflection of only -3.4 mm. The 80° case has an initial peak tip deflection of 14.6 mm at 80 seconds, a steady state deflection of

10mm. Transverse tip velocities show both cases to be stable and vibrations dying out in approximately 1000 seconds. FFT of the velocities are shown in Figure 34 and reveal that multiple natural frequencies are being excited with the dominant frequency being the tip mode, 0.809 Hz.

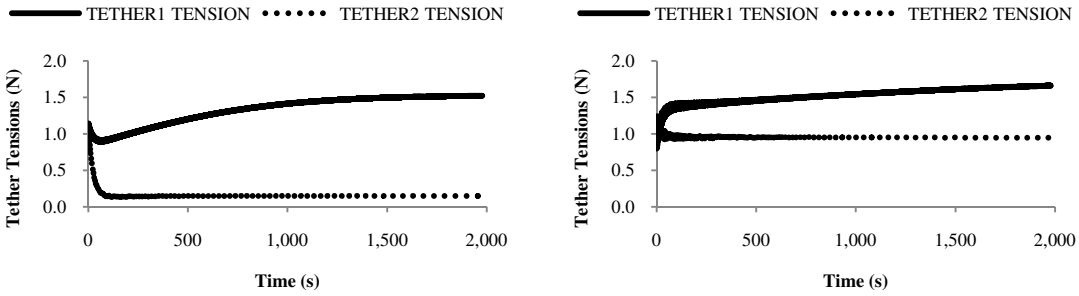

Figure 31. HPSA3 tether tension histories for 0˚ (left) and 80˚ (right) incident angles

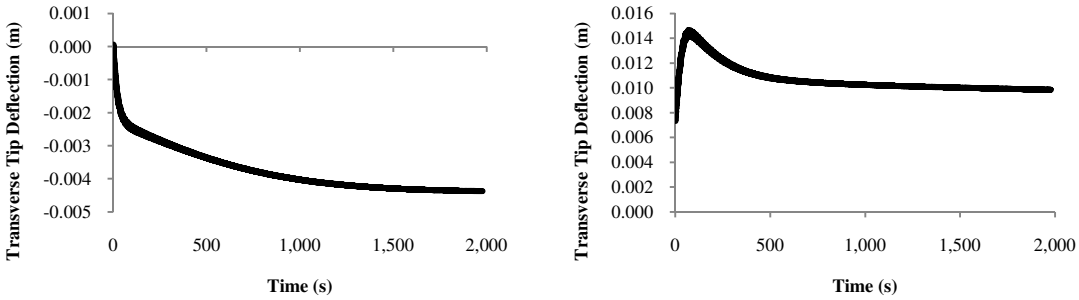

Figure 32. HPSA3 tip displacement histories for 0˚ (left) and 80˚ (right) incident angles

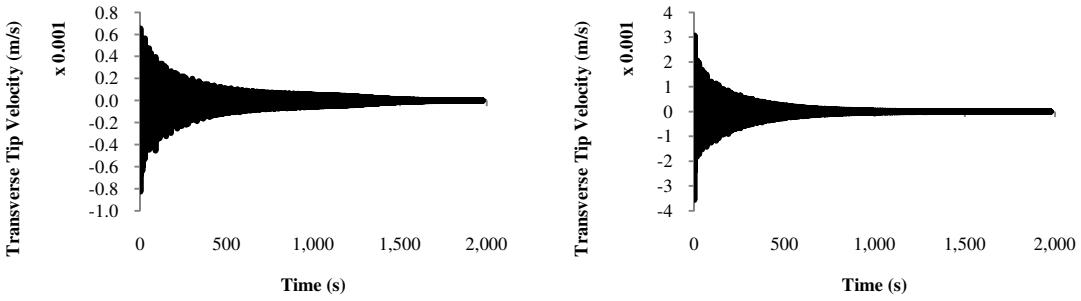

Figure 33. HPSA3 tip velocity histories for 0˚ (left) and 80˚ (right) incident angles

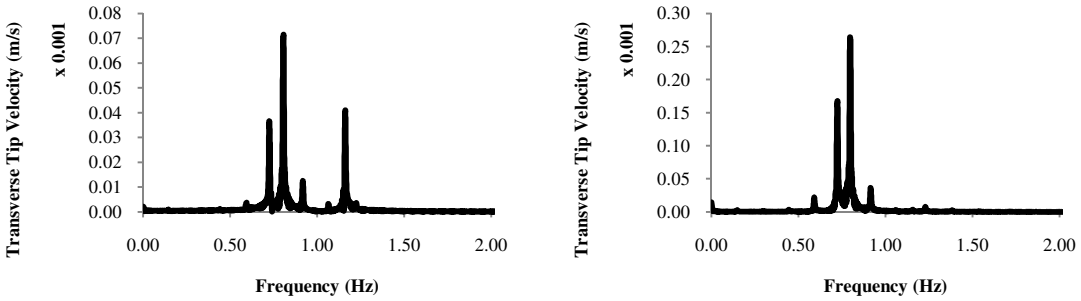

Figure 34. HPSA3 tip velocity FFTs for 0˚ (left) and 80˚ (right) incident angles

5.3.4. Comparison

Each of the wing configurations are compared using the transverse tip velocity Fast Fourier Transform plots by means of their dominant frequencies and amplitudes. Visual examination of the transverse tip velocity history plots also clarifies whether the system is stable or unstable. The comparative results can be seen in Table 8. Dominant amplitude and frequencies from the FFT's are shown in the first two rows. These results are then nondimensionalized in the 3rd and 4th rows for a better means of comparison. Amplitudes are nondimensionalized by dividing by the HST at 0˚amplitude.

Frequencies are nondimensionalized by being multiplied by the thermal time constant from shown in (20) similar to those in section 5.1.

Table 8. Comparison between wing configurations

	HST		SSE		HPSA2		HPSA3	
	0°	80°	0°	80°	0°	80°	0°	80°
FFT Peak Velocity Amplitude (m/s)	8.49E-03	1.68E-03	4.63E-02	1.39E-02	3.18E-03	3.05E-04	7.10E-05	2.64E-04
FFT Peak Velocity Frequency (Hz)	0.095	0.095	0.032	0.032	0.023	0.536	0.807	0.796
Nondimensional FFT Peak Velocity Amplitude	1.00	0.20	5.45	1.64	0.37	0.04	0.01	0.03
Nondimensional FFT Peak Velocity Frequency	2.26	2.26	0.72	0.72	0.51	12.00	18.06	17.79
Stable	yes	no	no	no	no	yes	yes	yes

SSE proves to be the worse design with the highest amplitudes and lowest frequencies of vibration excluding the HPSA2 case where the tether goes slack. As stated earlier, its nondimensional frequency is relatively close to one which means more damping is required to maintain stability. However, HPSA3 outperforms the other configurations having the highest dominant frequency, lowest amplitude vibration, and is stable for all incident angle cases performed.

5.4. Effects of Damping on HPSA Transient Response

The effect of damping on the HPSA wing configurations is further analyzed by performing additional transient cases. Previous cases assumed damping for ζ=0.01%. To better understand HPSA's sensitivity to damping, a magnitude above and below the previous value of damping was considered, ζ=0.1% and ζ=0.001% respectively. Both

HPSA designs (HPSA2 and HPSA3) are evaluated with these damping ratios for 0˚ and 80˚ incident angle cases, so a total of eight additional transient cases are performed.

Time histories for HPSA2 are shown in Figure 35 and Figure 36. With a slack tether, the effects of damping on the 0˚ incident angle case are insignificant. Both cases remain unstable, and follow a similar path. At 80˚ for HPSA2, the effects of damping are more pronounced with amplitudes dying out at a slower rate for the ζ=0.001% case.

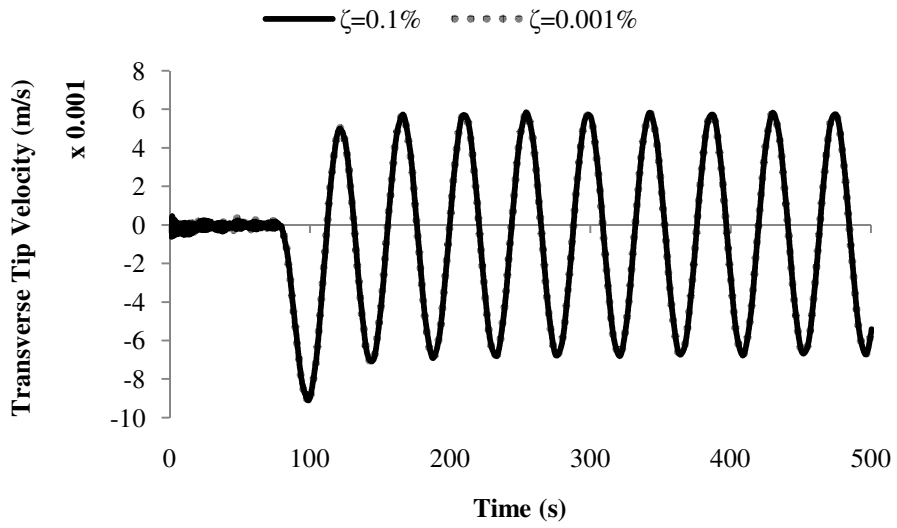

Figure 35. Tip velocity history for HPSA2 with 0˚ incident angle applied

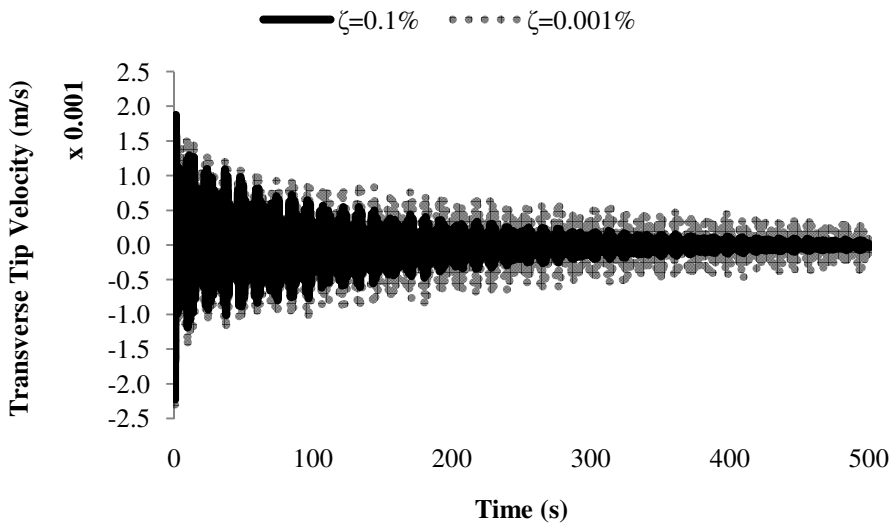

Figure 36. Tip velocity history for HPSA2 with 80˚ incident angle applied

Time histories for HPSA3 (presented in Figure 37 and Figure 38) show similar behavior to the HPSA2 at 80˚ incident angle case. Considering that the damping values vary over a range of two magnitudes and amplitudes only differ slightly, the HPSA design proves to be only mildly sensitive to damping. This is again attributed to the HPSA design having the periods of its tip frequencies far enough away from the time constant (or its nondimensional frequency not equal to one). Therefore, thermal loading does not sync up with a natural frequency and cause instability.

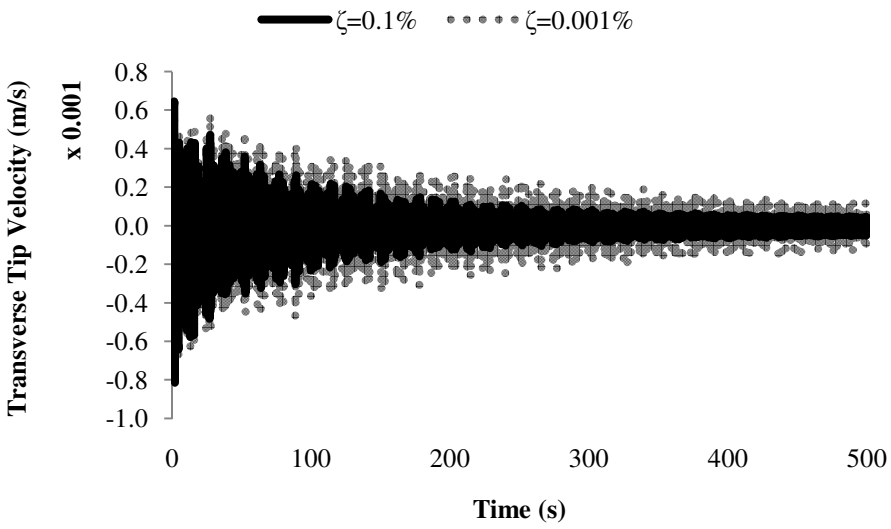

Figure 37. Tip velocity history for HPSA3 with 0˚ incident angle applied

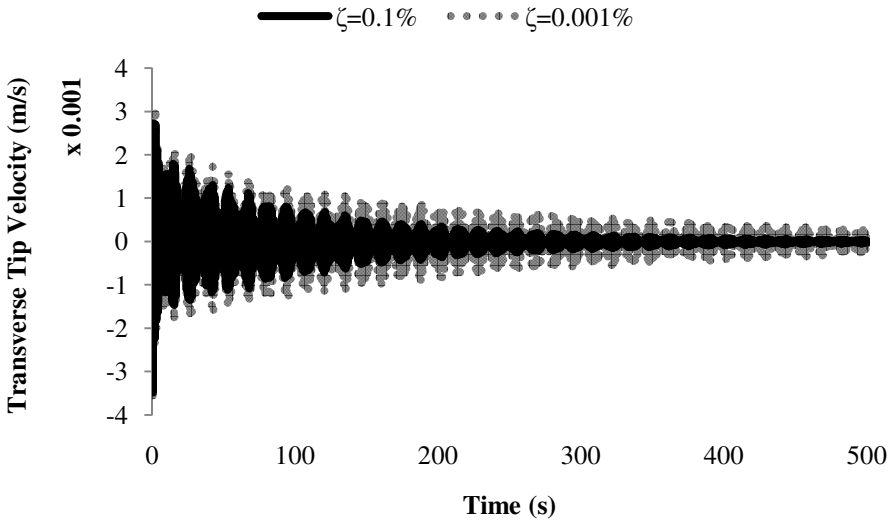

Figure 38. Tip velocity history for HPSA3 with 80˚ incident angle applied

6. CONCLUSIONS AND RECOMMENDATIONS

6.1. Conclusion

- While straight STEM wing dynamics are dominated by the effects of temperatures through the cross section, bow STEM wings are heavily reliant on the additional effects of the average temperatures on STEM and tether lengths.
- The additions of tethers and bowing of the STEM can reduce the steady state tip deflection by over two magnitudes if tethers remain taut.
- HPSA Configuration 3 outperforms the Hubble Space Telescope, the HPSA Straight STEM Equivalent, and HPSA Configuration 2. Under unidirectional radiant heating, it has higher excitation frequencies, lower amplitudes of vibration, and remains stable over a large range of incident angles, and requires little damping to remain stable. Therefore, *the High Power Solar Array design can outperform its straight STEM counterparts with respect to thermal-structural stability under unidirectional solar radiant heating.*

6.2. Recommendations

- An analytical model of the HPSA wing should be created.
- A stability analysis should be performed and criteria found for developing a stable HPSA wing.
- A 3D model of the HPSA wing should be created to investigate possible instabilities, including torsion of the wing along its center axis.
- A 3D model of a HPSA assembly should be created to investigate possible instabilities, including modes which could excite multiple wings simultaneously.

REFERENCES

[1] Mac Naughton J. D., 1963, “Unfurlable Metal Structures for Space Exploration,” American Astronautical Society -- Advances in Astronautical Sciences, **13**, pp. 217-246.

[2] Stribling R., 2006, “Boeing High Power Thin Film Solar Array,” American Institute of Aeronautics and Astronautics Inc., San Diego, CA, United States, pp. 124-146.

[3] Augusti G., 1968, “Instability of Struts Subject to Radiant Heat,” Meccanica, **3**(3), pp. 167-176.

[4] Beam R. M., 1969, "On the Phenomenon of Thermoelastic Instability (Thermal Flutter) of Booms with Open Cross Section", Technical Note No. D-5222, Ames Research Center, Mofett Field, Calif.

[5] Yu Y.-Y., 1969, “Thermally Induced Vibration and Flutter of a Flexible Boom,” Journal of Spacecraft and Rockets, **6**(8), pp. 902-910.

[6] Merrick V. K., 1970, "Instability of Slender Thin-Walled Booms Due to Thermally Induced Bending Moments", Technical Note No. D-5774, NASA, Washington, D.C.

[7] Frisch H. P., 1970, "Coupled Thermally-Induced Transverse Plus Torsional Vibrations of a Thin-Walled Cylinder of Open Section", Technical Report No. R-333, Goddard Space Flight Center, Greenbelt, Maryland.

[8] Murozono M., and Sumi S., 1989, “Thermally Induced Bending Vibration of Thin-Walled Boom Caused by Radiant Heating,” Memoirs of the Faculty of Engineering, Kyushi University, **49**(4), pp. 273-290.

[9] Thornton E. A., and Kim Y. A., 1993, “Thermally-Induced Bending Vibrations of a Flexible Rolled-up Solar-Array,” Journal of Spacecraft and Rockets, **30**(4), pp. 438-448.

[10] ANSYS, 2004, “ANSYS, Inc. Theory Reference,” User Reference Manual Version 9.0, (November), p. 1067.

[11] ANSYS, 2005, “ANSYS Coupled-Field Analysis Guide,” User Reference Manual Version 10.0, (August), p. 273.

[12] Carroll J., and Oldson J., 1995, “Tethers for Small Satellite Applications,” AIAA/USU Small Satellite Conference, Logan, Utah.

[13] MatWeb™, 2010, “DuPont ™ Kevlar ® 29 Aramid Fiber,” Matweb™.

[14] Tomlin D. D., Faile G. C., Hayashida K. B., Frost C. L., Wagner C. Y., Mitchell M. L., Vaughn J. A., and Galuska M. J., 1997, "Space Tethers : Design Criteria", Technical Memorandum No. 108537, Marshall Space Flight Center, MSFC, Alabama.

[15] Cengel Y. A., 2003, *Heat Transfer: A Practical Approach*, McGraw-Hill, Boston.

[16] MatWeb™, 2010, “DuPont ™ Kapton ® 50HN Polyimide Film , 13 Micron Thickness,” Matweb.

VITA

Shawn Avery Hagler received his Bachelor of Science degree in mechanical engineering along with a minor in business administration from Texas A&M University in December of 2006. Shawn continued on to graduate school at Texas A&M University in January 2007 and graduated with his M.S. in December of 2010. Shawn's research has been under the guidance of Dr. Alan Palazzolo. His focus has been on structural dynamics of flexible space structures and finite elements. Shawn can be reached through the Texas A&M Mechanical Engineering Department:

c/o Dr. Alan Palazzolo

Department of Mechanical Engineering

3123 TAMU

College Station, TX 77843-3123

His email is shawnhagler@gmail.com